

Formulating and Deploying Strength Amplification Controllers for Lower-Body Walking Exoskeletons

Gray C. Thomas^{1,*}, Orion Campbell², Nick Nichols², Nicolas Brissonneau³,
Bingham He³, Joshua James², Nicholas A. Paine² and Luis Sentis^{3,*}

¹ The University of Michigan, USA

² Apptronik Inc., USA

³ The Human Centered Robotics Lab, The University of Texas at Austin, Austin, USA

Correspondence*:

Gray Thomas / Luis Sentis

gcthomas@umich.edu / lsentis@austin.utexas.edu

2 ABSTRACT

3 Augmenting the physical strength of a human operator during unpredictable human-directed
4 (volitional) movements is a relevant capability for several proposed exoskeleton applications,
5 including mobility augmentation, manual material handling, and tool operation. Unlike controllers
6 and augmentation systems designed for repetitive tasks (e.g. walking), we approach physical
7 strength augmentation by a task-agnostic method of force amplification—using force/torque
8 sensors at the human–machine interface to estimate the human task force, and then amplifying
9 it with the exoskeleton. We deploy an amplification controller that is integrated into a complete
10 whole-body control framework for controlling exoskeletons that includes human-led foot transitions,
11 inequality constraints, and a computationally efficient prioritization. A powered lower-body
12 exoskeleton is used to demonstrate behavior of the control framework in a lab environment.
13 This exoskeleton can assist the operator in lifting an unknown backpack payload while remaining
14 fully backdrivable.

1 INTRODUCTION

15 Exoskeletons offer the potential to greatly augment the physical load carrying ability by placing the strength
16 of machines under the dexterous control of people. But the amplification of strength through force sensor
17 feedback remains a challenging problem in practice. This problem is unique to this application area and
18 is rarely discussed with regard to the various other types of exoskeletons—*e.g.* those that aim to recover
19 locomotion capability lost to disease (Kwa et al., 2009; Agrawal et al., 2017), offload the strenuous work
20 of rehabilitation therapy from therapists (Sugar et al., 2007; Kim and Deshpande, 2017), or aid healthy
21 locomotion with timed power boosts (Mooney et al., 2014; Zhang et al., 2017; Sawicki et al., 2020).
22 Amplification control systems are designed to magnify the physical strength of the operator as he or she
23 interacts with a load *through the exoskeleton*, while also reducing the weight and inertia the operator feels
24 from the exoskeleton itself. This kind of control allows non-repetitive, unpredictable tasks with unknown
25 payloads.

26 Lifting *known* payloads is a simpler problem. These loads can be lifted by directly compensating
27 their nominal weight with actuator torque commands (*i.e.* the “gravity compensation” strategy). This
28 compensation could be lifting mostly the exoskeleton itself (Kazerooni et al., 2005), or even offloading
29 the operator’s own bodyweight (Kong et al., 2010; Lv et al., 2018; Lin et al., 2019). In an exoskeleton
30 system that can be easily backdriven by the operator, gravity compensation alone is a practical approach
31 for lifting well-modeled payloads (Campbell, 2018). However, the operator must still accelerate the full
32 inertia, compensate for any model error, and lift any extra payloads. The inertia burden can be lessened by
33 adding positive acceleration feedback (Kazerooni, 2005; Kong and Tomizuka, 2009), but all three issues
34 can be addressed by adding force-feedback-based amplification.

35 Admittance control for exoskeletons (Yu and Rosen, 2013; Fontana et al., 2014; Jacobsen and Olivier,
36 2014; Lecours et al., 2012) uses force sensor feedback at the human interface¹ in order to increase the
37 human-side closed-loop admittance, reduce sensitivity to the mass model, and lift unknown loads. But the
38 admittance ‘increase’ is relative to the admittance controller’s plant: a position-controlled robot. Since
39 position-controlled robots have an artificially low admittance to begin with (Yu and Rosen, 2013; Gonzalez
40 and Asada, 2019), the closed-loop human-side admittance is typically not an improvement over the torque-
41 controlled gravity compensation strategy. Additionally, the position-controlled plant of the admittance
42 controller will attenuate all external forces acting on the robot. This has the disadvantage of depriving the
43 operator of the force feedback they would normally perceive when they interact with the load.

44 In order to allow bidirectional transmission of forces to coexist with amplification of human strength,
45 the exoskeleton must transmit both amplified forces from the user to the load and attenuated forces from
46 the load to the user. And this requires a force sensor configuration that can distinguish between load-
47 and human-originated forces. Directly measuring a robot–load interface and robot–human interface with
48 force sensors allowed (Kazerooni and Guo, 1993; Kazerooni and Mahoney, 1991a,b) to control *disparate*
49 admittance behaviors for each interface.² But the controller from (Kazerooni and Guo, 1993) was still not
50 designed to improve the human-side admittance relative to the torque-controlled gravity compensation
51 strategy. It still used admittance control and a position-controlled robot. In this paper, we use force sensing
52 at the human–exoskeleton and actuator–exoskeleton interfaces (*i.e.* series elastic actuators), and this
53 serves the dual purposes of distinguishing the human from the load and allowing torque control at the
54 joints. The two interface admittances are then shaped with a cascade of amplification feedback on top of
55 torque-controlled actuators.³

56 Unfortunately, the problem of non-passivity is inherent to feedback control that conceals inertia. This is
57 an issue regardless of how the inertia was concealed—through positive acceleration feedback (Kazerooni,
58 2005) or force feedback (Buerger and Hogan, 2007). Without passivity, we must fall back to robust
59 control in order to certify such behaviors. Most importantly, the exoskeleton’s human-facing port—its
60 force–position relationship at the human–exoskeleton interface—will be in a feedback interconnection with
61 the human’s exoskeleton-facing port. Studies of this feedback interconnection (Kazerooni, 1990; Buerger
62 and Hogan, 2007, 2006; He et al., 2019) and the human in particular (He et al., 2019; He et al., 2020) have
63 modeled the human as a mass-spring-damper system with a range of parameter values. The most variable
64 parameter is stiffness, as this depends on muscle contraction (Hogan, 1984). We must demonstrate that no
65 possible human behavior leads to instability—a robust control problem. Designing a machine to be passive

¹ Measuring human muscular effort, as can also be accomplished via electromyography (muscle measurement) (Kawamoto and Sankai, 2005; Young and Ferris, 2016).

² The HARDIMAN I exoskeleton (Makinson et al., 1969) attempted to do this as well, but with a flawed approach that neglected multi-joint coordination.

³ Our reaction-force sensing series elastic actuators are torque controlled based on disturbance observers (Paine et al., 2014; Paine, 2014).

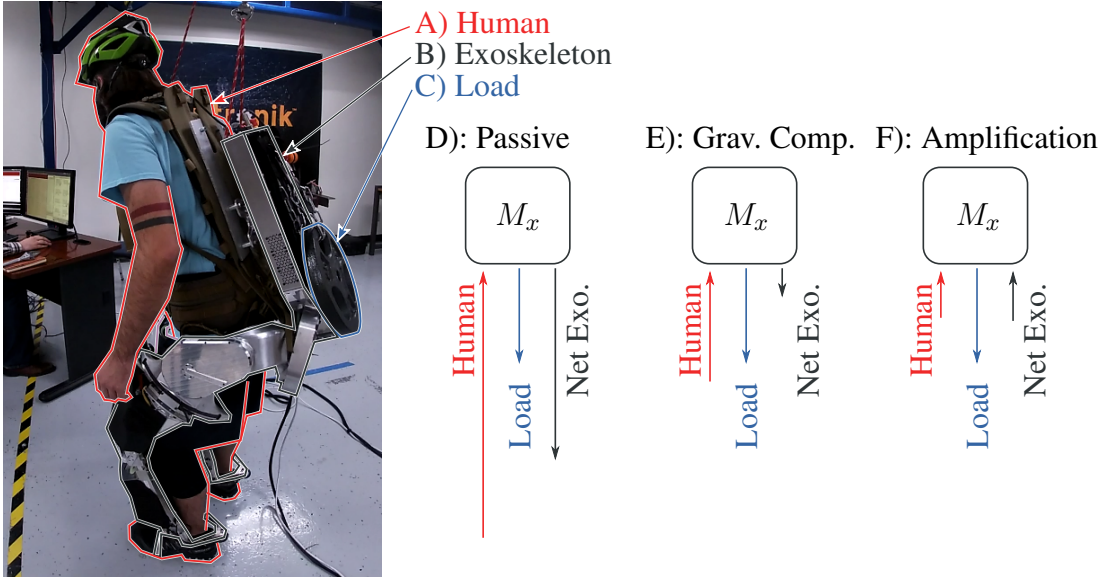


Figure 1. Human–exoskeleton–load interaction illustrating the concept of amplification. Marker A, the Human (inc. part of the backpack), connects to B, the Apptronik Sagittarius Exoskeleton, which connects to C, the unknown Load. The Human–Exoskeleton connection is force/torque sensitive to allow human force feedback. Three diagrams represent forces acting on the inertia matrix of the exoskeleton M_x in static equilibrium. When the exoskeleton is in zero-torque mode, the human supports both the load and the gravitational weight of the exoskeletons (D). When the exoskeleton compensates gravity, the human needs only compensate the load and the gravity compensation error (E). Amplification improves on this by making the exoskeleton augment the human input, in addition to compensating gravity (F).

66 (Colgate and Hogan, 1988; Hogan, 1989; Colgate and Brown, 1994; Adams and Hannaford, 1999) can also
 67 be seen as a robust control problem: such designs guarantee stability against a very wide range of ‘human’
 68 behaviors—the set of all passive transfer functions. Our prior work (Thomas et al., 2019; He et al., 2019;
 69 He et al., 2019; He et al., 2020) has studied this stability problem for a table-mounted elbow exoskeleton.

70 In this paper, we deploy an amplification controller on a 12 degree of freedom (12-DOF) lower-body
 71 exoskeleton with 8 torque-controlled active joints and 4 passive (but sensorized) joints (Fig. 1). The
 72 core framework of this controller is a multi-joint coordination approach modeled after humanoid robot
 73 controllers for torque-controlled joints (Sentis et al., 2010; Kim et al., 2016) (e.g. the Valkyrie robot at
 74 NASA JSC (Radford et al., 2015; Paine et al., 2015)) in which a list of ‘tasks’ (e.g. the position of the end
 75 effector, or the force between the feet) is accomplished by the robot. The full controller comprises (a) an
 76 optimization that determines robot joint torques using a *prioritized* list of tasks and a set of constraints that
 77 act on the sum of human and robot torques—the ‘Shared-Body Controller’ (Sec. 5); (b) a six degree of
 78 freedom (6-DOF) task that constrains the robot to follow human-led footstep transitions—the *inter-foot*
 79 force task (Sec. 4); (c) an amplification task that accomplishes strength amplification in Cartesian space
 80 (Sec. 2); and (d) a heuristic tuning strategy for the amplification filter, which is based on (He et al., 2019)
 81 and (Thomas et al., 2019) (Sec. 3). We demonstrate the deployed controller’s ability to reduce the human
 82 effort necessary to lift the robot itself and an unknown payload, as well as the operator’s ability to easily
 83 back-drive the system to walk around and climb some stairs (Sec. 6).

Symbol	Meaning
M_x, B_x, g_x	exoskeleton mass matrix, Coriolis vector, and gravity vector
\ddot{q}, \dot{q}, q	exoskeleton joint acceleration, velocity, and position vectors
τ	exoskeleton joint torque vector
J_h, f_h	human interaction cuff Jacobian, forces
J_l, f_l	load interaction Jacobian, forces
J_t, x_t	task Jacobian, position
\bar{J}_t	dynamically consistent pseudo-inverse of J_t
Λ_t	Task-space inertia matrix
\hat{f}_t	desired task force
α	human strength amplification rate
\hat{f}_a	Ideal (infinite bandwidth) desired amplification force
$\hat{f}_a(t), \hat{F}_a(s)$	desired amplification task force vector (time domain, frequency domain)
$f'_h(t), F'_h(s)$	transformed human force (time domain, frequency domain)
$K(s)$	Force feedback filter

Table 1. Nomenclature for Sec. 2

2 STRENGTH AMPLIFICATION TASK

84 Strength amplification can be illustrated using the example of an ideal fixed-base (arm-like) “exoskeleton”
 85 performing a force-feedback behavior with an end effector in contact with both the human and some load.

86 Consider a fully actuated, grounded base exoskeleton acted on by both a human operator (Jacobian J_h ,
 87 and force f_h) and an unknown load (Jacobian J_l , and force f_l) (list of symbols in Tab. 1),

$$M_x(q)\ddot{q} + B_x(q, \dot{q}) + g_x(q) = \tau + J_h^T f_h + J_l^T f_l. \quad (1)$$

88 The exoskeleton measures the human forces, f_h , and can use this measurement to specify τ . As we will
 89 see, by implementing an amplifying control law, the exoskeleton can reduce the human’s perception of the
 90 load. However to define this amplification law, we will need to first introduce the concept of a whole-body
 91 control task (Sentis et al., 2010).

92 Whole body control tasks describe behaviors we want a robot to achieve, for example moving an end
 93 effector to a desired 6-DOF pose in Cartesian space. Tasks can also specify the desired internal forces of
 94 multi-contact (Kim et al., 2016). More generally, tasks define both an effort-flow port of the robot and a
 95 target behavior for the robot to imitate at that port—a spring-damper behavior for position control and a
 96 force behavior for force control. This port is known as the task-space. By using the mapping between the
 97 joint-space of the robot and the task-space position x_t (and the mapping’s Jacobian, J_t), a whole-body
 98 controller can implement the task behaviors even while floating in zero gravity or maintaining contact with
 99 arbitrarily shaped ground (Sentis et al., 2010).

100 We define the amplification task to reduce human perception of load and exoskeleton dynamics
 101 disturbances in the task space. These task-space dynamics are originally (*i.e.* in open-loop) found by
 102 premultiplying (1) by $(J_t M_x^{-1} J_t^T)^{-1} J_t M_x^{-1}$, yielding

$$\Lambda_t(\ddot{x}_t - \dot{J}_t \dot{q}) + \bar{J}_t^T (B_x + g_x) = \bar{J}_t^T (\tau + J_h^T f_h + J_l^T f_l), \quad (2)$$

103 where $\Lambda_t = (J_t M_x^{-1} J_t^T)^{-1}$ is the task-space mass matrix and $\bar{J}_t = M_x^{-1} J_t^T \Lambda_t$ is the dynamically
 104 consistent pseudo-inverse of the task Jacobian (Kim et al., 2016). The amplification task specifies only a
 105 linear subspace of the torque vector, $\bar{J}_t^T \tau$, as

$$\bar{J}_t^T \tau = \hat{f}_a + \bar{J}_t^T(g_x), \text{ where } \hat{f}_a = (\alpha - 1) \bar{J}_t^T J_h^T f_h. \quad (3)$$

106 Here, the first term \hat{f}_a represents a desired force amplifying the human operator's strength, and the second
 107 term compensates gravity. Reduced human perception of load and exoskeleton dynamic disturbances can
 108 be seen in the closed-loop task-space,

$$\frac{1}{\alpha} \Lambda_t(\ddot{x}_t - \dot{J}_t \dot{q}) + \frac{1}{\alpha} \bar{J}_t^T(B_x) = \bar{J}_t^T J_h^T f_h + \frac{1}{\alpha} \bar{J}_t^T J_l^T f_l. \quad (4)$$

109 While the human term stays the same, every other term is reduced. Equivalently, we could say these
 110 closed-loop dynamics amplify the influence of the human force by a factor of α . But this behavior is
 111 complicated by the matrices $\bar{J}_t^T J_h^T$ and $\bar{J}_t^T J_l^T$, which represent projection onto the space of the task as
 112 well as the potential for mismatch between the reference frames of the task, the human-measuring cuff
 113 interface, and the load.

114 In the special case where the human and load forces act *only* in the task-space and the human and load
 115 forces are expressed in the units and reference frame of the task-space (*i.e.* $J_t = J_h = J_l$), this simplifies
 116 to

$$\Lambda_t(\ddot{x}_t - \dot{J}_t \dot{q}) + \bar{J}_t^T(B_x) = \alpha f_h + f_l, \quad (5)$$

117 which clearly shows the human advantage with respect to the load, inertia, and Coriolis forces. For example,
 118 this case occurs if (1) both forces are applied to one sensorized, 6-DOF end effector; (2) the sensor
 119 measurements of the spatial force vectors of the human and the load are all converted to the same reference
 120 frame (Featherstone, 2014); and (3) this frame is also the frame in which the task is expressed.

121 This law is unfortunately an unobtainable ideal, because it changes the apparent inertia the human feels
 122 instantaneously. In other words, the law requires that the actuation bandwidth is infinite. Beyond the
 123 actuation bandwidth, all feedback systems asymptotically revert to their natural dynamics. Thus, in the
 124 limit as frequency approaches infinity, the frequency-domain representation of exoskeleton torque should
 125 be zero.

126 2.1 Filtered Amplification Task

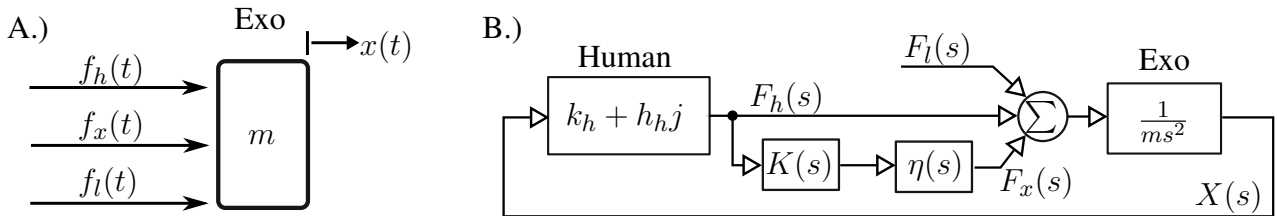
127 To allow for bandwidth limited amplification tasks, we introduce the notion of filtered force feedback
 128 amplification. Instead of an amplification task following Eq. (3), we define a desired filtered amplification
 129 force as the result of a frequency domain filter as

$$\hat{F}_a(s) = K(s) F'_h(s), \quad \text{where} \quad f'_h(t) = \bar{J}_t^T J_h^T f_h, \quad (6)$$

130 f'_h is the human force vector represented in the task space, $F'_h(s)$ is its Laplace transform, and $K(s)$ is
 131 some matrix of linear filters analogous to $(\alpha - 1)$ in the ideal case. We design this matrix of filters to be
 132 diagonal, and consider a strategy for tuning the diagonal filter elements in Sec. 3.

133 In our exoskeleton, the *amplification task* is a 6-DOF task concerning the exoskeleton's hip/backpack
 134 frame and the 6-axis force/torque sensor that connects the hip/backpack link to the operator. The vector
 135 $F'_h(s)$ is the 6-axis force/torque sensor measurement's expression in the task frame (the exoskeleton's hip

Symbol	Meaning
m	one-DOF exoskeleton mass
$k_h + h_{hj}$	human complex stiffness (see (He et al., 2020))
$x(t), X(s)$	one-DOF position (time-domain, frequency-domain)
$f_l(t), F_l(s)$	load force
$f_x(t), F_x(s)$	exoskeleton actuator force
$f_h(t), F_h(s)$	human force
$\hat{\alpha}(s)$	desired amplification transfer function
$\alpha(s)$	realized amplification transfer function
$K(s)$	feedback controller transfer function
$\eta(s)$	actuation imperfections (time-delay, low-pass filtering)
ω_a	amplification bandwidth (tuning parameter)
α_0	steady-state amplification rate
ζ	amplification damping ratio

Table 2. Nomenclature for Sec. 3**Figure 2.** Amplification filter tuning model, a one-DOF mass (m) acted upon by human (f_h), exoskeleton actuator (f_x), and load (f_l) forces (A). Closed loop system resulting from complex stiffness human mechanical impedance and exoskeleton amplification with bandwidth-limiting time-delay and low pass filter effects in $\eta(s)$ (B).

frame). And $\hat{F}_a(s)$ is the desired *amplification task* spatial force vector (expressed in hip frame), which will be treated as a time-domain vector signal $\hat{f}_a(t)$ in Sec. 5.

3 TUNING THE AMPLIFICATION FILTERS

Since ideal amplification cannot be attained, we must consider a design space of more realistic amplification behaviors. And the essence of this design space is a bandwidth limitation on the control. This bandwidth limit, and its impact on coupled human–exoskeleton stability, has been studied in the context of single degree of freedom exoskeleton systems (He et al., 2019; Thomas et al., 2019; Huang et al., 2020; He et al., 2020), and we will use the single degree of freedom case as a heuristic for understanding the tuning of the amplification task’s $K(s)$ filter elements in our multi-DOF exoskeleton. While this heuristic omits several obvious nonlinear effects and inter-task couplings in the full system, it captures the basic problem of human–exoskeleton instability that can occur when bandwidth limits are ignored.

3.1 Human-Exoskeleton Stability Model

Consider a 1-DOF linear human and exoskeleton system (Fig. 2.A, Tab. 2) where the exoskeleton acts like an inertia M and is being acted upon by three forces: the human $f_h(t)$, the actuator $f_x(t)$, and the load $f_l(t)$ as

$$m\ddot{x}(t) = f_l(t) + f_h(t) + f_x(t), \quad (7)$$

150 where $x(t)$ the shared position of the human and the exoskeleton. We write this model in the frequency
 151 domain as

$$ms^2X(s) = F_l(s) + F_h(s) + F_x(s), \quad (8)$$

152 using capitalization to distinguish Laplace transforms from time-domain versions of the same signal.

153 The force-feedback filter $K(s)$ is based on a nominal amplification behavior $\hat{\alpha}(s) = 1 + K(s)$.⁴ We
 154 parameterize the desired amplification transfer function as

$$\hat{\alpha}(s) = \frac{s^2 + 2\zeta\omega_z s + \omega_z^2}{s^2 + 2\zeta\omega_p s + \omega_p^2}, \quad (9)$$

155 i.e. a second order lag with two conjugate poles at lower frequency than the two conjugate zeros, using the
 156 same ζ twice for convenience, though this could potentially be optimized. While this $\hat{\alpha}(s)$ is not strictly
 157 causal, it produces a $K(s)$ which is:

$$K(s) = \hat{\alpha}(s) - 1 = \frac{2\zeta(\omega_z - \omega_p)s + \omega_z^2 - \omega_p^2}{s^2 + 2\zeta\omega_p s + \omega_p^2}. \quad (10)$$

158 Actuation imperfections ultimately limit the bandwidth, and we model these as the transfer function $\eta(s)$.
 159 They include a time delay T and low pass filter effect (i.e. the closed loop bandwidth of the actuator's
 160 torque controller) at frequency ω with damping ratio ζ ,

$$\eta(s) = e^{-Ts} \frac{\omega^2}{s^2 + 2\zeta\omega + \omega^2}. \quad (11)$$

161 The mechanical impedance of the human is also modeled as a complex stiffness—a spring with a
 162 dissipation term that does not change with frequency. (This model can be interpreted as similar to a spring
 163 with a coulomb friction term that scales with the magnitude of deflection, such that the energy lost in
 164 flexing the spring does not depend on the speed of the flexing (Brissonneau et al., 2021).) This complex
 165 stiffness model is more accurate than the viscous damping model in predicting human energy dissipation in
 166 the elbow, especially at low frequencies (He et al., 2020).

167 To facilitate easy tuning of our controller we reparameterize in terms of an amplification bandwidth
 168 parameter ω_a (equal to ω_p) and a low frequency amplification gain $\alpha_0 \geq 1$ (equal to ω_z^2/ω_p^2) so that

$$K(s) = \frac{2\zeta(\sqrt{\alpha_0} - 1)\omega_a s + (\alpha_0 - 1)\omega_a^2}{s^2 + 2\zeta\omega_a s + \omega_a^2}. \quad (12)$$

169 We then tune only the amplification bandwidth ω_a .

170 3.2 Tuning ω_a

171 The tuning process we propose is simple. Sufficiently low values of ω_a are always stable, so we can
 172 increase ω_a until instability to tune the system without explicit system identification.

173 The bode plot of $X(s)/F_l(s)$ ('System' in Fig. 3) transitions from a stable low-pass filter behavior to an
 174 unstable system as ω_a is increased. We note that the critical frequency satisfies a relationship akin to zero

⁴ We reserve the symbol $\alpha(s)$ for the realized amplification behavior, which includes the effect of actuator imperfections $\eta(s)$.

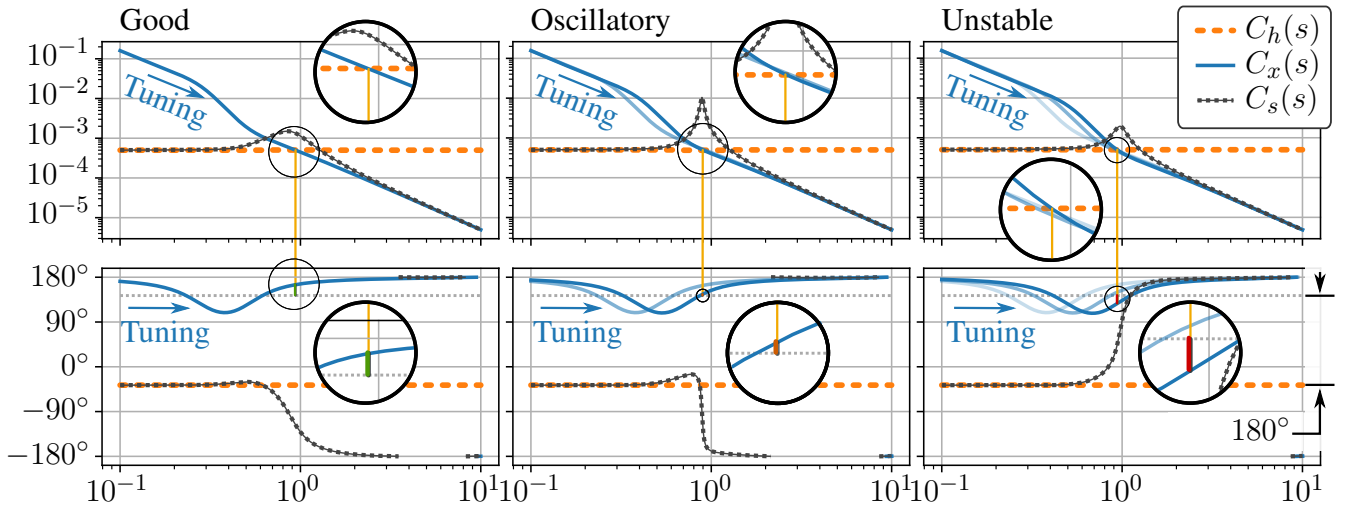


Figure 3. One parameter tuning of the amplification filter. Three bode plots show three different tuning configurations as the single tuning parameter (the amplification bandwidth ω_a) is increased to failure in our frequency domain model. Tuning arrows indicate increasing ω_a . Plotted are the (integral) admittance of the human, $C_h(s) = 1/(K_h + C_h j)$, the human-side admittance of the exoskeleton, $C_x(s) = 1/(\alpha(s)Ms^2)$, and the admittance of the closed loop system obtained when the two are interconnected in parallel, $C_s(s) = X(s)/F_l(s)$. Note that in the third plot, the phase of the closed loop system rises instead of falling, indicating an unstable pole in the right half of the complex plane. In all three bode plots, magnification is used to highlight the calculation of a “Human Phase Margin” which predicts this instability. This calculation uses the phase of $C_x(s)$ at the frequency where the magnitude of $C_x(s)$ is equal to the magnitude of $C_h(s)$ —the crossover frequency. At this frequency, stability of the resulting human–exoskeleton interconnection is determined by comparing the phase of $C_x(s)$ to a reference phase 180° offset from the phase of $C_h(s)$. The difference between the phase of $C_x(s)$ and this reference is the “Human Phase Margin.”

175 phase margin, where both the magnitude of the human (integral) admittance, $1/(K_h + C_h j)$ ('Human' in
 176 Fig. 3), is equal to that of the amplified exoskeleton admittance, $1/(\alpha(s)Ms^2)$ ('Robot' in Fig. 3), and the
 177 phases of the two are offset by 180° . We call the phase angle difference $\angle C_x(j\omega) - \angle C_h(j\omega) - 180^\circ$ at
 178 crossover frequency ω where $|C_x(j\omega)| = |C_h(j\omega)|$ the ‘Human Phase Margin’. Since the human phase
 179 margin is also the phase margin for the open loop transfer function $C_x(s)C_h^{-1}(s)$ (in the unit negative
 180 feedback case), the human phase margin predicts the stability of the closed loop system resulting from the
 181 human–exoskeleton interconnection.

182 A single tuning experiment can determine the limiting bandwidth for any particular amplification shape.
 183 Starting with ω_a very low, we slowly scale it up until the system appears to vibrate. Once the threshold of
 184 oscillation is found, the oscillation frequency is roughly the crossover frequency, and we could obtain an
 185 estimate of the human phase if we had a good model of the torque tracking performance and time delay.
 186 The problem is practically solved, however, by the formulation of the controller in a one-parameter tunable
 187 way. With one knob, it is easy to increase the performance up to the limit, back off for robustness, and get a
 188 good result in the end.

189 3.3 Practical Considerations

190 Ultimately this model is introduced as a heuristic for the tuning behavior occurring in the more complex
 191 exoskeleton system, so we now revisit its assumptions with an eye to the realistic case.

192 If a small value for α_0 is selected such that the minimum phase of $1/(\hat{\alpha}(s)Ms^2)$ stays above the gray
 193 line in Fig. 3, the system will be stable even for very high ω_a . However, this will not hold true forever,

194 and the bandwidth limiting factors in $\eta(s)$ will cause the realized behavior $1/(\alpha(s)Ms^2)$ itself to become
 195 unstable for high values of ω_a .

196 The human model considered here neglected human inertia. If this term were added, the human inertia
 197 would be roughly comparable to the inertia of the exoskeleton. The model would not be changed at low
 198 frequencies, so the base case (stability of low ω_a) of our tuning process would stay the same. The lower
 199 phase of the human due to the inertia would improve the maximum allowable ω_a , but a limit would still
 200 exist due to the bandwidth limiting factors in $\eta(s)$.

201 The inertia of the exoskeleton changes as the person moves it, and this means that the stability of the
 202 amplification behavior can change depending on the configuration. Practically, this means that when tuning
 203 for maximum performance, care will need to be taken to test each iteration of the ω_a parameter over a wide
 204 range of poses, to ensure a robust stability.

205 It is well known that humans have the ability to co-contract their antagonistic muscles and artificially
 206 raise their mechanical impedance, and this represents another changing aspect of this problem. If we
 207 assume that this scales both k_h and h_h together, as supported in (He et al., 2020), then co-contraction
 208 will lower the human admittance and improve the human phase margin. In fact, by using a co-contraction
 209 predictor learned from wearable sensors (*e.g.* EMG and bicep circumference sensors), we have been able to
 210 design controllers that adapt online to take advantage of co-contraction to improve controller performance
 211 (Huang et al., 2020). To ensure robust stability while tuning for performance, the operator will need to
 212 avoid co-contraction so as to explore the gain-limiting case.

4 INTER-FOOT FORCE TASK

213 Human-led foot contact transitions, such as walking or shifting balance, are an important part of any scheme
 214 for controlling lower-body exoskeletons. To allow this critical feature we introduce a second task, the
 215 *inter-foot force task*, that is achieved simultaneously and causes the exoskeleton to follow human-initiated
 216 foot lifting.

217 With one foot on the ground, this foot acts as a virtual base for the exoskeleton—a contact constraint on
 218 its otherwise free-fall dynamics. Since the exoskeleton is not designed to jump, we can assume that some
 219 sort of virtual base always exists. When two feet are on the ground at the same time, we can imagine a
 220 virtual single foot between them that acts like a base and moves between the feet according to the operator’s
 221 own weight distribution.

222 Two feet together have 12-DOF worth of reaction forces, and the virtual single foot contact only allows
 223 6-DOF to be used as a virtual base. The remaining 6-DOF can be thought of as an error, representing the
 224 mismatch between the exoskeleton’s reaction force distribution and the operator’s. This error should be
 225 zero, and eliminating it is the purpose of the *inter-foot force task*.

226 To define this error, we first consider how correct reaction force distribution looks, and then consider
 227 the linear space of reaction forces perpendicular to this. For this purpose, we introduce an optimization
 228 problem that optimally distributes a net reaction wrench f_s into two components, one for each foot,

$$\underset{f_1, f_2}{\text{minimize}} \quad \frac{f_1^T Q_1 f_1}{2} + \frac{f_2^T Q_2 f_2}{2} \quad (13)$$

$$\text{subject to} \quad {}^s X_1^* f_1 + {}^s X_2^* f_2 = f_s, \quad (14)$$

Symbol	Meaning
f_i	foot i 's spatial force vector in frame $i \in \{1, 2\}$
f	stacking of f_1 and f_2
f_s	sum of foot spatial force vectors in frame s
Q_1, Q_2, Q	reaction force cost definition matrices
${}^b X_a^*$	spatial force vector transform, frame $a \rightarrow$ frame b
λ	Lagrange multiplier vector in optimization
X	equality constraint matrix in optimization
Γ	$= [XQ^{-1}X^T]^{-1}$
\bar{X}	$= Q^{-1}X^T\Gamma$, a pseudo-inverse of X
f_d	<i>inter-foot force task</i> error in frame d
\tilde{X}	weighted inter-foot difference matrix
\mathbf{G}	virtual base definition matrix

Table 3. Nomenclature for Sec. 4

229 where Q_1 and Q_2 are positive definite and typically diagonal. We introduce two new reference frames:
 230 frame s (for “sum”), and frame d (for “difference”). Both frames are weighted averages of the two foot
 231 frames. Frame s is approximately matched with the human center of pressure. Frame d is the mirror image
 232 of frame s , and both frames overlap at the mid-foot point when the human puts equal weight on each foot.
 233 Transformation ${}^s X_1^*$ converts spatial force vectors from the 1st foot's frame to frame s , and ${}^s X_2^*$ is the
 234 same for the other foot. The force f_s represents the sum of the two foot spatial force vectors expressed in
 235 frame s (Tab. 3).

236 The equality constrained quadratic programming problem can be solved analytically. Starting from the
 237 equilibrium conditions,

$$Qf + X^T\lambda = 0, \quad \text{where,} \quad (15)$$

$$Q = \begin{pmatrix} Q_1 & \\ & Q_2 \end{pmatrix}, \quad (16)$$

$$f = \begin{pmatrix} f_1 \\ f_2 \end{pmatrix}, \quad (17)$$

$$X = \begin{pmatrix} {}^s X_1^* & {}^s X_2^* \end{pmatrix}, \quad \text{and} \quad (18)$$

$$Xf = f_s. \quad (19)$$

238 In matrix form,

$$\begin{pmatrix} Q & X^T \\ X & 0 \end{pmatrix} \begin{pmatrix} f \\ \lambda \end{pmatrix} = \begin{pmatrix} 0 \\ f_s \end{pmatrix}, \quad (20)$$

$$\begin{pmatrix} f \\ \lambda \end{pmatrix} = \begin{pmatrix} Q^{-1} - \bar{X}XQ^{-1} & \bar{X} \\ X^T & -\Gamma \end{pmatrix} \begin{pmatrix} 0 \\ f_s \end{pmatrix}, \quad (21)$$

239 where $\Gamma = [XQ^{-1}X^T]^{-1}$ and $\bar{X} = Q^{-1}X^T\Gamma$. Thus

$$f = (Q^{-1}X^T) \cdot [XQ^{-1}X^T]^{-1}f_s, \quad (22)$$

$$\begin{pmatrix} f_1 \\ f_2 \end{pmatrix} = \begin{pmatrix} Q_1^{-1s} X_1^{*T} \\ Q_2^{-1s} X_2^{*T} \end{pmatrix} \cdot [{}^s X_1^{*T} Q_1^{-1s} X_1^{*T} + {}^s X_2^{*T} Q_2^{-1s} X_2^{*T}]^{-1} f_s. \quad (23)$$

240 This 12-DOF solution f is the virtual single foot contact's distribution of reaction forces between the
 241 two feet. The other six degrees of freedom in the foot forces—the degrees of freedom not specified by
 242 constraint (14)—represent the *inter-foot force task* error. More specifically, we define the *inter-foot force*
 243 *task* error f_d in frame d to complete a parameterization of the foot forces f

$$f = \bar{X}f_s + \left[I - \bar{X}(\bar{X}^T \bar{X})^{-1} \bar{X}^T \right] \tilde{X}^T f_d, \quad (24)$$

244 where we introduce

$$\tilde{X} = \begin{pmatrix} {}^d X_1^{*-1} w_2 \\ -{}^d X_2^{*-1} w_1 \end{pmatrix}, \quad (25)$$

245 as a rough parameterization of the deviation from the desired force distribution. This gets contorted into
 246 being perpendicular to \bar{X} by the premultiplication with an \bar{X} image space nullifier. As will be described
 247 in Sec. 5.5, the *inter-foot force task* puts a penalty on $\|f_d\|$, and when $f_d = 0$, reaction forces minimize
 248 the previously defined quadratic cost (since $f = \bar{X}f_s$). This leaves f_s as the path of least resistance the
 249 optimization uses to hold up the weight of the exoskeleton.

250 We define \mathbf{G} to simplify notation:

$$f = \mathbf{G} \cdot \begin{pmatrix} f_s \\ f_d \end{pmatrix}, \quad (26)$$

251

$$\mathbf{G} = \left(\bar{X} \quad \left[I - \bar{X}(\bar{X}^T \bar{X})^{-1} \bar{X}^T \right] \tilde{X}^T \right). \quad (27)$$

252 As mentioned in Sec. I, our exoskeleton controller is tasked with *simultaneously* accomplishing the
 253 *amplification task* at the hip/backpack interface (Sec. 3) and the *inter-foot force task*. In terms of reaction
 254 forces, the *amplification task* serves a similar purpose to the centroidal momentum task introduced in
 255 (Koolen et al., 2016) or the center of mass task in (Sentis et al., 2010): it determines the required *sum*
 256 of reaction forces. Meanwhile, the *inter-foot force task* (similar to the internal force tasks from (Kim
 257 et al., 2016)) determines the part of the reaction force vector that is decoupled from the center of mass
 258 acceleration. With both tasks active, the reaction forces are all defined and the joint torques can be thought
 259 of as resulting from an inverse dynamics process—as in the Dynamic Balance Force Control of (Stephens
 260 and Atkeson, 2010).

5 WEIGHTED 1-NORM SHARED-BODY CONTROL

261 To combine the *amplification task* and *inter-foot force task* while also respecting limitations on the
 262 exoskeleton, we compute the joint torques of the exoskeleton using a linear optimization problem. This
 263 problem uses concepts of contact constraints, prioritization between task sub-components, a weighted
 264 1-norm cost, and the actuator-mapped reaction force space in order to be computationally efficient.

Symbol	Meaning
τ	optimization variable: joint torque vector
M_x, B_x, g_x	exoskeleton mass, Coriolis, gravity
\ddot{q}, \dot{q}, q	joint acceleration, velocity, position
S	underactuation matrix for a free floating base
J_h, f_h	Jacobian for human contact and forces
J_r, f_r	Jacobian for ground contact and reaction forces
C_r, c_r	reaction force inequality matrix and bias
$e(\cdot)$	a task error function
$\sigma(\cdot)$	a task scalarization function
s_+, s_-	1-norm slack variables
w	weight vector
J_a, f_a, \ddot{x}_a	Jacobian, force, accel. for the <i>amplification task</i>
J_f, f_f, \ddot{x}_f	Jacobian, force, accel. for feet
$\mathbf{J}, \mathbf{f}, \mathbf{\ddot{x}}$	Jacobian, force, accel. for composite task
$\bar{\mathbf{J}}$	Dynamically consistent pseudo-inverse of \mathbf{J}
Λ	inertia matrix in composite task frame
\mathbf{G}	virtual base definition matrix
$\bar{\tau}$	maximum torque, human + exoskeleton
\hat{f}_a	vector of filtered desired <i>amplification task</i> forces from Sec. 2

Table 4. Nomenclature for Sec. 5265 **5.1 Contact Constraints**

266 There is an important caveat to this concept of a virtual single-foot contact. Unlike actual fixed-base
 267 robots, exoskeletons with feet can topple over. Since an exoskeleton is essentially a humanoid robot (in
 268 feedback interconnection with a human), the inequality-constrained floating base models (Koolen et al.,
 269 2016; Kim et al., 2016, 2018; Mungai and Grizzle, 2020) are still relevant to keeping its feet flat on the
 270 ground. These constraints act on the base–ground reaction forces, f_r , which are not part of the standard
 271 *fixed-base* robot model. They are defined by the combination of a *floating-base* exoskeleton and a contact
 272 constraint:

$$M_x \ddot{q} + B_x + g_x = S\tau + J_h^T f_h + J_r^T f_r + J_l^T f_l, \quad (28)$$

$$J_r \ddot{q} + \dot{J}_r \dot{q} = 0, \quad (29)$$

273 with notation as in Tab. 4. To avoid tilting the feet, sliding the feet, or pulling on the ground, additional
 274 inequality constraints must be maintained,

$$C_r f_r + c_r \geq 0. \quad (30)$$

275 The inequalities described by C_r and c_r are simple approximations of the friction cone: for example, two
 276 rows would be used to express $\mu|f_x| \leq f_z$, where μ is the friction coefficient. But the size of C_r depends
 277 on how many feet are on the ground. In addition to these limits due to contact, there are upper bounds to
 278 the torque magnitude the exoskeleton can provide. And if some of the joints are not actuated, then they
 279 have an upper limit of zero.

280 **5.2 Actuator-Mapped Reaction Force Space**

281 In order to speed up the solver and increase its accuracy, we reduce the number of free variables in our
 282 optimization problem by handling some equality constraints in advance. This is not necessary theoretically,
 283 as the problem is not actually changed by handling these constraints, however attempts to lean on the
 284 solver's own ability to perform linear algebra resulted in disappointing precision and speed. Thus, we found
 285 the need to quickly re-express reaction forces as functions of joint torque.

286 More specifically, we find $(f_a(\tau)^T, f_f(\tau)^T)^T$ —the mapping from the 12-DOF joint torque vector to
 287 an 18-DOF vector of forces that concatenates the ground reaction forces with the human–exoskeleton
 288 interaction forces at the backpack.⁵ We define a new composite Jacobian, \mathbf{J} , force vector, \mathbf{f} , and task
 289 acceleration, $\ddot{\mathbf{x}}$, as

$$\mathbf{J} = \begin{pmatrix} J_a \\ J_f \end{pmatrix}, \quad \mathbf{f} = \begin{pmatrix} f_a \\ f_f \end{pmatrix}, \quad \ddot{\mathbf{x}} = \begin{pmatrix} \ddot{x}_a \\ \ddot{x}_f \end{pmatrix}. \quad (31)$$

290 Beginning with the physical equations (28) and (29), we can reformat the dynamics of the exoskeleton as
 291 a matrix equality with an analytic solution,

$$\begin{pmatrix} M_x & \mathbf{J}^T \\ \mathbf{J} & 0 \end{pmatrix} \begin{pmatrix} \ddot{q} \\ -\mathbf{f} \end{pmatrix} = \begin{pmatrix} -B_x - g_x \\ \ddot{\mathbf{x}} - \mathbf{J}\dot{q} \end{pmatrix} + \begin{pmatrix} S \\ 0 \end{pmatrix} \tau, \quad (32)$$

292 which can be solved as in (21). The S matrix represents the under-actuation due to the floating base
 293 (under-actuation due to non-actuated mechanical joints is handled separately, through joint torque limits).
 294 We define the dynamically consistent pseudo inverse of \mathbf{J}^T , $\bar{\mathbf{J}}^T$, satisfying $\bar{\mathbf{J}}^T \mathbf{J}^T = I$ (a left inverse), but
 295 likely *not* satisfying $\mathbf{J}^T \bar{\mathbf{J}}^T = I$:

$$\bar{\mathbf{J}}^T = (\mathbf{J} M_x^{-1} \mathbf{J}^T)^{-1} \mathbf{J} M_x^{-1}. \quad (33)$$

296 And we define inertia in the composite task frame $\Lambda = (\mathbf{J} M_x^{-1} \mathbf{J}^T)^{-1}$. Together, these allow us to state the
 297 result,

$$\mathbf{f} = \Lambda \ddot{\mathbf{x}} - \Lambda \mathbf{J} \dot{q} + \bar{\mathbf{J}}^T (B_x + g_x) - \bar{\mathbf{J}}^T S \tau. \quad (34)$$

298 Some terms in the previous expression are more significant than others, and some of the less significant
 299 terms are also corrupted by both imperfect knowledge of the exoskeleton's mass matrix and (filtered)
 300 differentiation noise inherent in using quantized position sensors to estimate velocity and acceleration
 301 estimates. We did not notice a significant drawback in switching to a simplified version which represents a
 302 steady state equilibrium:

$$\mathbf{f} = \bar{\mathbf{J}}^T (g_x - S \tau). \quad (35)$$

303 Of course, if we moved fast enough, these omissions would be noticeable. With this simplification, swinging
 304 the swing foot very fast should require the operator to resist the centrifugal extension of the knee due to the
 305 inertia of the exoskeleton. Also, squatting very quickly should result in a non-zero backpack sensor force
 306 due to the neglected acceleration terms. However, at the speeds we tested these effects were dwarfed by
 307 other control and mechanical imperfections. We hope that future exoskeletons will achieve such mastery
 308 over the basic terms that these dynamic terms will regain relevancy.

⁵ Ultimately we only care about the 12-DOF vector of the *inter-foot force task* error and *amplification task* error, $(f_a(\tau)^T, f_d(\tau)^T)^T$ but the 18-DOF vector representation was more intuitive to debug. We will use the \mathbf{G} matrix to obtain $f_d(\tau)$ from $f_f(\tau)$ later.

309 **5.3 Prioritized Tasks**

310 With multiple tasks and inequality constraints, the exoskeleton’s behavior is often over-specified. For
 311 example, the combination of the lateral (y-axis force) component of the *amplification task*, the mediolateral-
 312 plane rotation (x-axis torque) component of the *amplification task*, and the stance-foot’s lateral center-of-
 313 pressure limitation may require a non-zero task error. This is easy to visualize if the exoskeleton’s hip is
 314 far from the stance foot: the ground reaction force can point toward the hip and avoid rotation, or it can
 315 point straight up and avoid lateral force, but it cannot do both simultaneously. A more general version
 316 of this problem is well known in the humanoid robotics community (Bretl and Lall, 2008). This happens
 317 frequently during dynamic walking. And it demands that we specify not only which tasks we want to
 318 achieve, but in which order the task sub-components should fail to be satisfied if they conflict in this way.⁶

319 When constraints become active, there is neither an obvious choice for what to give up nor an analytical
 320 method to optimally decide. However, if we provide a *prioritization* of the task sub-components, then an
 321 optimal answer exists. This prioritization requires additional parameters—a rank order for each task sub-
 322 component—but these are relatively few, and easy to understand and adjust. This approach has also been
 323 used to handle redundancy in task definition even without the limitation of constraints (Sentis et al., 2010).
 324 When constraints become active, the prioritization approach simply abandons the task sub-components
 325 one at a time, starting with the least important, until the problem is solvable. The lowest priority task
 326 sub-components are the ones for which we feel the human will have the easiest time comfortably handling
 327 the task sub-component failure. In the case of our *amplification task*, this could mean a failure to amplify
 328 the interaction force and/or a failure to achieve gravity compensation. In the case of our *inter-foot force*
 329 *task*, it could mean applying a force to the user’s swing foot (failure to gravity compensate) or failing to
 330 match the user’s desired contact force distribution (failure to transition appropriately, most evident if a foot
 331 is load-bearing when it should not be).

332 Strict prioritization between the tasks is a mathematically well-defined optimization scheme known as
 333 lexicographic optimization (Bouyarmane and Kheddar, 2017). Lexicographic problems must be solved as a
 334 series of related optimization sub-problems. First, the most important cost must be optimized within the
 335 problem constraints—the first optimization sub-problem. Next, the second most important cost must be
 336 optimized within both the original problem constraints and a new constraint. This new constraint requires
 337 that the previously minimized cost for the most important objective stays at its previously determined
 338 optimal value. With a solution to this second optimization sub-problem, a lexicographic optimization
 339 would proceed forward one cost at a time, solving optimization sub-problems with an ever-increasing list
 340 of constraints. And this recursive process will continue until each component of the prioritized list of costs
 341 has been optimized in its own sub-problem.

342 In our hardware, we could only solve three lexicographic optimization sub-problems within our one
 343 millisecond real-time control window, so with 12 prioritized task sub-components, a proper lexicographic
 344 solution was outside the realm of plausibility.

345 **5.4 Weighted 1-Norm Cost**

346 Weighted scalarization costs are an established approach to approximating a lexicographic optimization in
 347 the context of humanoid control (Bouyarmane and Kheddar, 2017). To avoid our computational bottleneck,
 348 we also used a scalarization that retains the linearity of the cost function. But in doing so we must add

⁶ After trying both prioritizations, we determined that the operator prefers a failure in x-axis torque balance, even if this causes the exoskeleton’s hip to “wobble” relative to the human’s with every step due to the compliance of the backpack attachment in this degree of freedom.

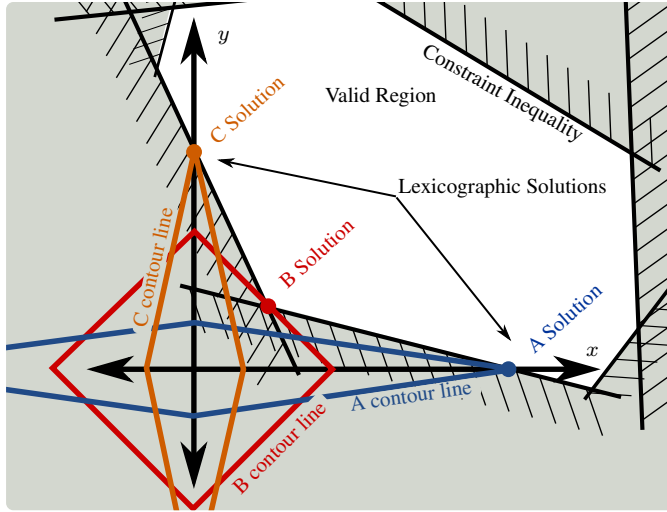


Figure 4. Illustration of how weighted 1-norm costs can behave similarly to lexicographic (prioritized) costs. Plot in the space of task error for task- x and task- y . Weighted 1-norm costs A, B, and C are depicted with a single contour line each. Optimal solutions for each task shown as colored circles. The so-called “sparsity promoting” nature of the weighted 1-norm cost can be understood in this context as optimal solutions which sacrifice one task to achieve the other. As exemplified by cost B, however, this is not guaranteed and depends on the inequality constraints and the shape of the valid region they generate.

349 two positive slack variables and two inequality constraints for each scalarized cost (which were all task
 350 elements) to remain within a linear programming framework. For our vector of task errors $e(\tau)$, we define
 351 a vector of scalarizations $\sigma(\tau)$

$$\sigma(\tau) = s_+ + s_- \quad \text{where} \quad s_+ \geq e(\tau), \quad \text{and} \quad s_- \geq -e(\tau), \quad (36)$$

352 where s_+ , and s_- are the newly introduced vector slack variables, and the new vector inequalities in
 353 (36) are elementwise inequalities. Under conditions that are almost always met,⁷ $\sigma(\tau) = |e(\tau)|$ (as an
 354 elementwise absolute value).

355 This approach to modelling an absolute value function within the confines of a linear programming
 356 problem is the key to our application of a weighted 1-norm cost on the vector of all task errors. Clearly,
 357 summing the elements of $\sigma(\tau)$ results in the vector 1-norm of $e(\tau)$. Summing the elements of $\sigma(\tau)$ with
 358 positive weightings (setting cost equal to $w^T \sigma(\tau)$ for some vector of positive weights w) is a weighted
 359 scalarization in the sense of (Bouyarmane and Kheddar, 2017), but we can also think of it as a weighted
 360 1-norm—as the 1-norm for a scaled version of the original space. We prefer this as a name for the way it
 361 invokes a lozenge-like rhomboid geometry in 2D, and a diagonally-scaled octahedron geometry in 3D.

362 To capitalize on this 2D intuition, Fig. 4 illustrates how the weighted 1-norm cost can be adjusted through
 363 the weighting to approximate different lexicographic costs (there are only two in 2D space: either x matters
 364 more than y or vice versa). The illustration features a convex 2D set of solutions which satisfy constraints.
 365 The two axes represent orthogonal tasks, with the origin representing zero error for both tasks. Cost A
 366 uses a weighting that penalizes y error more than the x , cost B penalizes them roughly equally, and cost C
 367 penalizes x error more than y . In both cases A and C, the minimum cost point which satisfies constraints
 368 falls on one of the two axes—exactly as a lexicographic solution would. The fact that 1-norm costs tend

⁷ Specifically that each element of $\sigma(\tau)$ appears in the cost with a strictly positive weight, and that $\sigma(\tau)$, s_- , and s_+ are otherwise decoupled from the problem.

369 to produce solution vectors with many zero entries (so-called “sparse” solutions (Candes et al., 2008))
 370 is well known and frequently exploited. To promote *lexicographic solutions* instead of simply solutions
 371 with many zeros requires tuning the penalty weights to favor the prioritized tasks. In our illustration, the
 372 weightings in A and C are sufficiently extreme, and two lexicographic solutions emerge. Cost B illustrates
 373 a non-lexicographic middle-ground: neither cost is penalized enough to completely dominate the other, and
 374 the solution vector assigns non-zero error to both tasks.

375 One disadvantage of weighted 1-norm costs in exoskeleton control is that the constraints are continuously
 376 varying due to the changing exoskeleton geometry, and this can cause the optimal behavior to jump
 377 discontinuously. This can occur if the 1-norm cost discontinuously switches from being aligned with one
 378 lexicographic solution to a different lexicographic solution or even a non-lexicographic solution. We call
 379 these abrupt switches “priority inversion events.” To avoid these events entirely, we would need 1-norm
 380 weights with near-infinite scale differences between task sub-components. Since this is obviously not
 381 possible with floating-point numbers, the weighted 1-norm is an approximation: it sacrifices accuracy
 382 for speed. Fortunately, the approximation of the lexicographic problem is asymptotically perfect as the
 383 weight discrepancy increases. We exploited large differences in the weights to avoid priority inversion
 384 events during our experiment. The numerical precision of the linear program solver allowed us sufficient
 385 space to set these weights orders of magnitude apart and achieve reliable reproduction of the lexicographic
 386 problem in practice. These numerical limits restrict the total number of priority levels that can be correctly
 387 implemented.

388 5.5 A Linear Program for Shared-Body Control

389 At this point, we can express the optimization problem that the shared-body controller needs to solve at
 390 every controller update. Note that the passive joints⁸ are treated as being active joints for the purpose of the
 391 optimization. Their non-zero torques represent the expectation of the exoskeleton on the human operator.

392 We write our optimization problem,

$$\underset{\tau, s_+, s_-}{\text{minimize}} \quad w^T s_+ + w^T s_- \quad (37a)$$

$$\text{subject to} \quad C_r f_r(\tau) \geq 0, \quad (37b)$$

$$\tau \leq \bar{\tau}, \quad -\tau \leq \bar{\tau}, \quad (37c)$$

$$s_+ \geq e(\tau), \quad s_+ \geq 0, \quad (37d)$$

$$s_- \geq -e(\tau), \quad s_- \geq 0, \quad (37e)$$

393 with some new notation from Tab. 4. Slack variables s_+ and s_- are introduced to describe absolute value
 394 operations. Weightings w form the weighted 1-norm cost. Limits on absolute torque are expressed with $\bar{\tau}$.
 395 And the τ -dependent vector $f(\tau)$ from (38) (or from the steady-state approximation (39)) is used to find
 396 $e(\tau)$ and $f_r(\tau)$.

397 The first, $e(\tau)$, represents the 12-DOF vector of task errors for the *amplification task* and *inter-foot force
 398 task*:

$$e(\tau) = \begin{pmatrix} f_d(\tau) - 0 \\ f_a(\tau) - \hat{f}_a \end{pmatrix}, \quad (38)$$

⁸ The exoskeleton has 2 passive DOFs per leg: ankle inversion/eversion (ankle roll) and internal/external rotation of the hip (hip yaw).

399 where \hat{f}_a is the desired amplification task force from (6) in Sec. 2.1; $f_a(\tau)$ is the force the exoskeleton
 400 applies at the backpack interface, which is a part of $f(\tau)$ as written in (31); and $f_d(\tau)$ is also related to
 401 $f(\tau)$ as in (26):

$$\begin{pmatrix} f_s(\tau) \\ f_d(\tau) \end{pmatrix} = \mathbf{G}^{-1} f_f(\tau), \quad (39)$$

402 using the matrix \mathbf{G} from (27).

403 The second, $f_r(\tau)$, represents the subset of the foot forces $f_f(\tau)$ corresponding to the feet that are actually
 404 on the ground. This vector is used to compute the constraints associated with hard friction cones and
 405 unilateral contacts—i.e. (30), which is directly reproduced in (37b).

406 We call this program “Shared-Body Control” because the human and the exoskeleton’s torque and contact
 407 forces are both relevant. The true conditions for tipping over the foot are a function of both human and
 408 exoskeleton reaction forces. The sum of the human and exoskeleton reaction forces needs to lie within the
 409 friction cone, but sometimes the human works to counterbalance large torques the exoskeleton applies to
 410 the ground. We cannot know the human forces given our sensor configuration, so we are forced to be either
 411 optimistic (risking failure) or very conservative. Taking the conservative route means that our constraint
 412 will occasionally interfere with our tasks unnecessarily.

413 The human is also the only possible source of torques for the passive joints. By relaxing the torque
 414 requirements on the passive joints, the optimization will produce a torque vector representing a sum of
 415 exoskeleton and human originated torques. While we cannot expect the human to implement such torques,
 416 we can use this technique to prevent the exoskeleton from abandoning tasks which it could accomplish
 417 with help from the human (bounded, of course, by $\bar{\tau}$).

6 IMPLEMENTATION IN HARDWARE

418 6.1 Hardware

419 Our hardware platform is the Sagittarius P5 lower-body exoskeleton from Apptronik Systems, shown in
 420 Fig. 5. This exoskeleton has 12 joints, six per leg. We name the joints in the serial kinematic chain from
 421 the torso to the foot 1) hip abduction/adduction, 2) hip flexion/extension, 3) hip internal/external rotation
 422 (hip yaw), 4) knee flexion/extension, 5) ankle flexion/extension, and 6) ankle pronation/supination (ankle
 423 roll). Of these six, four are powered joints. The two passive joints are hip internal/external rotation (also
 424 referred to as hip yaw for alignment with the local z axis) and ankle pronation/supination (which we also
 425 call ankle roll for similar reasons). The powered hip abduction and hip flexion joints are actuated by rotary
 426 series elastic actuators, while the other two feature proprietary linkage designs connecting linear series
 427 elastic actuators with rotary joint motion. Power is provided from off-board the device via a joint power
 428 and communication tether. The actuators communicate with a real-time Linux desktop workstation through
 429 an ethercat bus.

430 The different parts of the exoskeleton are highlighted in Fig. 5, with rigid bodies being bordered by
 431 different color lines on the spectrum from blue to purple, human attachment points in orange, and safety
 432 features in red. To ensure the safety of the operator, the exoskeleton is attached via a slack safety rope to
 433 an overhead gantry system, and the rope’s height is operated by an assistant when the height is changing
 434 rapidly (as in the stair-climbing activities pictured in Fig. 5. The operator wears a helmet, and there are
 435 multiple easy ways to stop the exoskeleton in an emergency: 1) a software emergency stop button, 2) a



Figure 5. The Apptronik Sagittarius Exoskeleton used in this paper. The operator can climb stairs with the exoskeleton, even when it is not amplifying forces, due to the backdrivable torque-controlled actuators (gravity compensation and strength amplification are both active in the pictured movement). Coloring segregates rigid exoskeleton parts for the right leg (blue-through-purple), human interfaces (orange) and the safety features (red).

436 button on the top of the main backpack circuitry box, and 3) a button that the operator is required to hold at
437 all times.

438 6.2 Controller Implementation

439 While we have presented the controller design in a very general way, not all of its nuanced behavior is
440 relevant enough to demand implementation in the hardware system we used. In particular, the dynamic
441 terms in (34) were not large enough for the operator to notice their omission, and the dynamically consistent
442 pseudo-inversion of \mathbf{J} is unnecessary given that \mathbf{J} is invertible with the tasks we defined, thus

$$\mathbf{f} = \mathbf{J}^{-T}(\mathbf{g}_x - S\tau). \quad (40)$$

443 Note that when a component of the *amplification task* has $K(s)$ set to zero, it will not amplify human
444 forces but will still compensate gravity.

445 We chose to amplify cuff forces at the hip/backpack sensor in order to assist the operator in lifting
446 a backpack-mounted payload. And as previously indicated, we applied a *inter-foot force task* to allow
447 the exoskeleton to switch ground contacts effectively. To summarize the tasks of the controller, the six
448 individual spatial force vector components of the human-side force are fed into a diagonal matrix of

amplification compensators as described in Sec. 3. And this occurs in the frame of the *amplification task*—the hip frame. For the three sagittal plane forces and torques (x -force, z -force, and y -torque) we may apply non-zero amplification, but the other three are left at zero in this work. This is based on the physical intuition that the sagittal plane forces and torque represent the larger interaction quantities during walking. This forms the 6-DOF *amplification task*. Based on a bed of 12 insole-mounted pressure sensitive resistors, a rough estimate of the human center of pressure is produced. This estimate is used to construct the elements of the *inter-foot force task*, which is also a 6-DOF task. With this hardware-specific preprocessing completed, the tasks are sent to a separate and more generic module to perform the linear programming optimization work. The software implementation of this optimization process is separate from the Apptronik control framework and is available as open source software (Thomas, 2019). It primarily acts as a wrapper layer for the linear programming solver from the COIN-OR (Lougee-Heimer, 2003) community.

6.3 Priorities

We avoided priority inversion events by iterative tuning of the priority weights (Tab. 5). This tuning was done with squatting and stepping behaviors similar to the planned tests. High-priority tasks that were never sacrificed held large weights, of roughly equal value. To effectively use the limited numerical precision, these tasks were equally ranked relative to each other. The most important weights were quickly identified and set to values that reliably avoided priority inversion in the tested behaviors. The more difficult question was identifying the priorities preferred by the operator.

We iterated various priority rankings between the components of the *amplification task* until our operator was satisfied with the behavior. First, we attempted to re-create linear inverted pendulum behavior by prioritizing the moment components over the force components. This prioritization had been effective with the Hume/Mercury biped robot (Kim et al., 2016, 2020). Unfortunately, this first approach frustrated the operator, as the exoskeleton was naturally unstable. We eventually settled on the weightings in Tab. 5, which sacrifice x -torque first and are more comfortable for the operator. This preference may be exoskeleton or operator specific. The main drawback of the priorities from Tab. 5 is that at each stance transition the hips of the device roll such that the stance hip is higher than the swing hip—likely due to the lower penalty on hip amplification x -torque. However, we must sacrifice something, and this appeared to be the least-uncomfortable choice. The large swing in the hip position is due to the rather loose coupling that the backpack provides in this degree of freedom.

In testing, we began to suspect that operators may prefer a lower task penalty on the *inter-foot force task* while in double support but react strongly negatively to *inter-foot force task* violation while in swing (since this entails the exoskeleton loading their swing foot). We made a slight modification to the sum scalarized cost for the *inter-foot force task* as described in (37a), (37d), (37e), and (38). A second copy of the task penalty was added, with a dead zone. We made the *inter-foot force task* error appear *twice* in the task error vector $e(\tau)$ instead of only once as in (38). Thus, we had two separate components of the weight vector w from (37a) that penalized the same task. To introduce the dead zone for the second copy of the penalty, we added a sparse bias vector to (37d) and (37e). We call this new penalty, with its dead zone and higher penalty cost, the “Limit Penalty” (see Tab. 5) since it acts like a soft limit forcing the values to stay within the dead zone. Within the dead zone, this new cost still behaves like the original weighted 1-norm cost (plus a constant bias that does not influence the optimum), but at the boundary of the dead zone, the weight suddenly becomes much higher.

Task	Weighting
Hip Amplification x -Force	1×10^5
Hip Amplification y -Force	1×10^5
Hip Amplification z -Force	1×10^5
Hip Amplification x -Torque	1×10^0
Hip Amplification y -Torque	1×10^1
Hip Amplification z -Torque	1×10^5
Inter-Foot x -Force, Limit Penalty	$1 \times 10^{-1}, 1 \times 10^5$
Inter-Foot y -Force, Limit Penalty	$1 \times 10^{-1}, 1 \times 10^5$
Inter-Foot z -Force, Limit Penalty	$1 \times 10^{-6}, 1 \times 10^6$
Inter-Foot x -Torque, Limit Penalty	$1 \times 10^{-6}, 1 \times 10^5$
Inter-Foot y -Torque, Limit Penalty	$1 \times 10^{-6}, 1 \times 10^5$
Inter-Foot z -Torque, Limit Penalty	$1 \times 10^0, 1 \times 10^5$

Table 5. Implemented Task Priorities

Test	SBC [†]	α_0	Load
6.4.1	Off	0	0 N
6.4.2	On	0	0 N
6.4.3	On	0	110 N
6.4.4	On	3	110 N

†—Shared-Body Controller (SBC) enabled.

Table 6. Experimental Parameters

491 We scheduled the dead zone width based on the center of pressure location, such that in single support
 492 this dead zone collapsed to zero and the *inter-foot force task* essentially took on the higher weighting of
 493 the limit penalty. In dual support, the width of the dead zone reached its widest when the feet were evenly
 494 balanced and reduced linearly in either direction away from that midpoint.

495 6.4 Demonstrating the Amplification Task

496 We conducted a set of simple tests to demonstrate the difference between gravity compensation and
 497 human strength amplification. These tests aimed to demonstrate an improvement in amplification stability
 498 relative to previous controllers developed for the exoskeleton and its previous partial prototypes (the 1-DOF
 499 testbed from (He et al., 2019; Thomas et al., 2019), a two degree of freedom leg, and a previous revision on
 500 the same lower-body design) under the same project (Campbell, 2018), which was a condition of our using
 501 the exoskeleton.⁹

502 Fig. 6 and Tab. 6 show the basic structure of our tests: the operator wears the exoskeleton in a roughly
 503 standing position and various controller features are turned on and off. Extra weight is attached to the
 504 backpack as an unknown load in tests 6.4.3-4, and the image shows where it hangs relative to the operator.
 505 Fig. 7 shows the results of the three tests.

506 In the first test, 6.4.1 the exoskeleton joints are on, but the desired torque is zero. The first column of
 507 plots in Fig. 7 show the large z -force on the backpack due to the gravitational load of the exoskeleton
 508 acting on the operator. Variation in the angle shows that the operator was not perfectly holding still over

⁹ Which is to say, our testing time was limited, and the scope of our experiments was narrow.

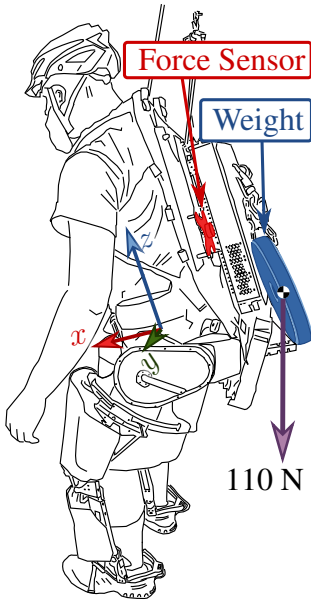


Figure 6. Load position in 6.4.3 and 6.4.4. Load hangs from a chain attached to the exoskeleton. Human effort measured with a six-axis force torque sensor, highlighted in red. Measurements are presented in the pictured “hip center” coordinate frame.

509 the duration of the test. This natural human movement, while it prevents us from easily comparing across
 510 experiments (the operator does not even have the same resting posture between loading configurations), is
 511 hard to compensate for or avoid.

512 The next test, 6.4.2 enables gravity compensation—which means the torques from the shared-body
 513 controller are applied to the exoskeleton, but the amplification filters are all set to apply no strength
 514 amplification feedback ($\alpha_0 = 1$, so $\hat{f}_a = 0$). This drastically reduces, but does not entirely eliminate,
 515 the interface forces and torques. Even if the exoskeleton’s mass parameters were perfectly modeled,
 516 the operator would still need to apply forces through this interface to control the passive joints of the
 517 exoskeleton. Compensating for the weight of the heavy exoskeleton is the most significant component of
 518 the system’s behavior. We can see this from the enormous reduction in human interface forces and torques
 519 in Fig. 7 between 6.4.1 and 6.4.2: the vertical force, F_z , drops roughly 300 Newtons, and the sagittal plane
 520 torque, T_y , drops roughly 40 Newton meters.

521 In test 6.4.3, we added an 11 Kg (25 lb) mass to the backpack, without changing the control mode.
 522 Based on our empirical determination, this represents the maximum load the exoskeleton could reliably
 523 handle without overheating during dynamic motions like walking. The test does not focus on the transient
 524 response but on the steady state behavior with the weight (mechanically, it would be hard to make the
 525 weight addition appear sudden without dropping it).

526 We see some unexpected behavior in the vertical sensor force: the weight’s 110 N did not transfer to
 527 the sensorized interface. The user confirmed that additional vertical force and sagittal torque were felt.
 528 This suggests a “force leak” in the design of the backpack sensor, where the force of the added weight
 529 is transferred to the operator without passing through the sensor. A likely culprit is the hip-pad of the
 530 backpack (directly connected to the operator) and the hips of the exoskeleton—as this would be consistent
 531 with the clear increase in the y -torque. The “force leak” does not appear to allow all vertical forces to
 532 bypass the sensor. 6.4.1 clearly shows large forces.

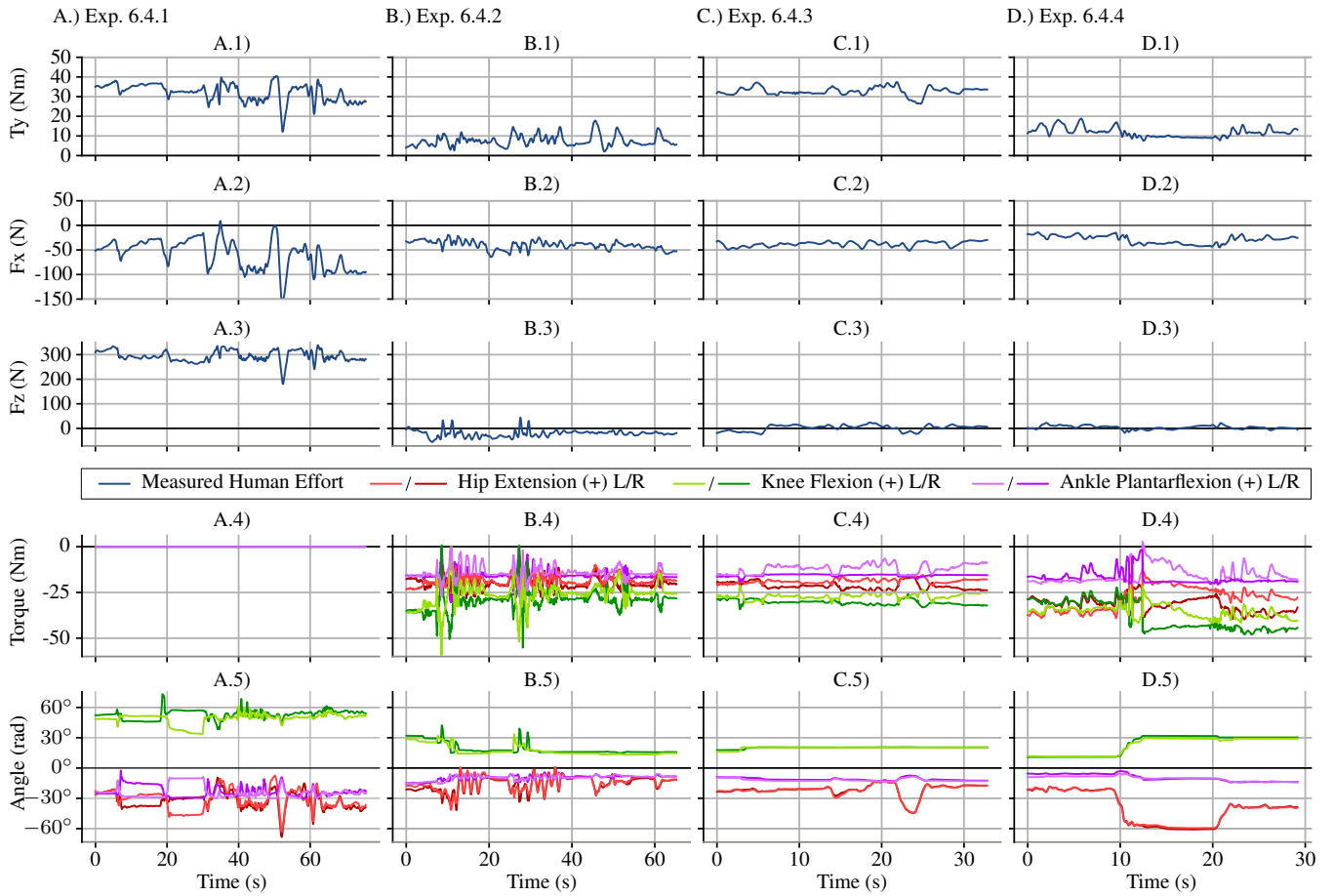


Figure 7. The four experiments from Tab. 6, shown as subfigure columns A–D, are compared in terms of the three sagittal plane components of the human–exoskeleton interaction force/torque, the sagittal joint torques, and the sagittal joint angles. In Exp. 6.4.1 (A), the exoskeleton joints apply no torque (as shown in A.4), and the human–exoskeleton interface supports ≈ 300 N (as shown in A.3) as well as a ≈ 35 Nm moment at the hip (as shown in A.1). In Exp. 6.4.2 (B), the controller is turned on with $\alpha_0 = 1$ (no amplification), and human–exoskeleton vertical force (B.3) and sagittal torque (B.1) are vastly decreased due to gravity compensation. In Exp. 6.4.3 (C), a 11 kg mass is attached to the back of the exoskeleton (as shown in Fig. 6), and this produces an increase in the human–exoskeleton sagittal torque (C.1), ≈ 30 Nm. Finally, Exp. 6.4.4 (D) increases α_0 from 1 (no amplification) to 3 in the sagittal tasks, and the human–exoskeleton sagittal torque increase due to the added mass is reduced by roughly a third—considering B.1, C.1, and D.1 representing the average numerical value of the curves, $D.1 - B.1 \approx 1/3(C.1 - B.1)$ —as expected. With the amplification engaged, the operator deepens the squat at 10 seconds (D.5) and then moves to a second, less extreme squat at 20 seconds (D.5), showing that the torque reduction continues to work. This squat is shown in the video attachment (Thomas, 2020). We would also expect that amplification would reduce the vertical force from the added mass; however, the vertical force remains roughly zero before adding the weight (B.3), after adding the weight (C.3), and with both the weight and amplification (D.3)—the expected 110 N force increase between (B.3) and (C.3) did not occur. Since the operator recalls feeling vertical forces from the addition of the mass, we suspect that there is a “force leak” where the vertical component transferred to the operator in a way the force sensor could not detect. Torque and angle measurements in the bottom two subfigure rows are measured using the exoskeleton’s spring deflection encoders and joint encoders, and therefore represent the exoskeleton’s—and not the operator’s—torque and position.

533 In the final test, 6.4.4, we engaged the amplification filters—providing a steady state amplification factor
 534 of 3, and a zero pair at 1 Hz for all three degrees of freedom in the sagittal plane. By choosing these
 535 conservative settings, we were able to achieve stability on the first try.¹⁰

¹⁰ A later gain-tuning experiment revealed that the bandwidth limit is higher than this, but we ran out of time for exhaustive identification of this limit.

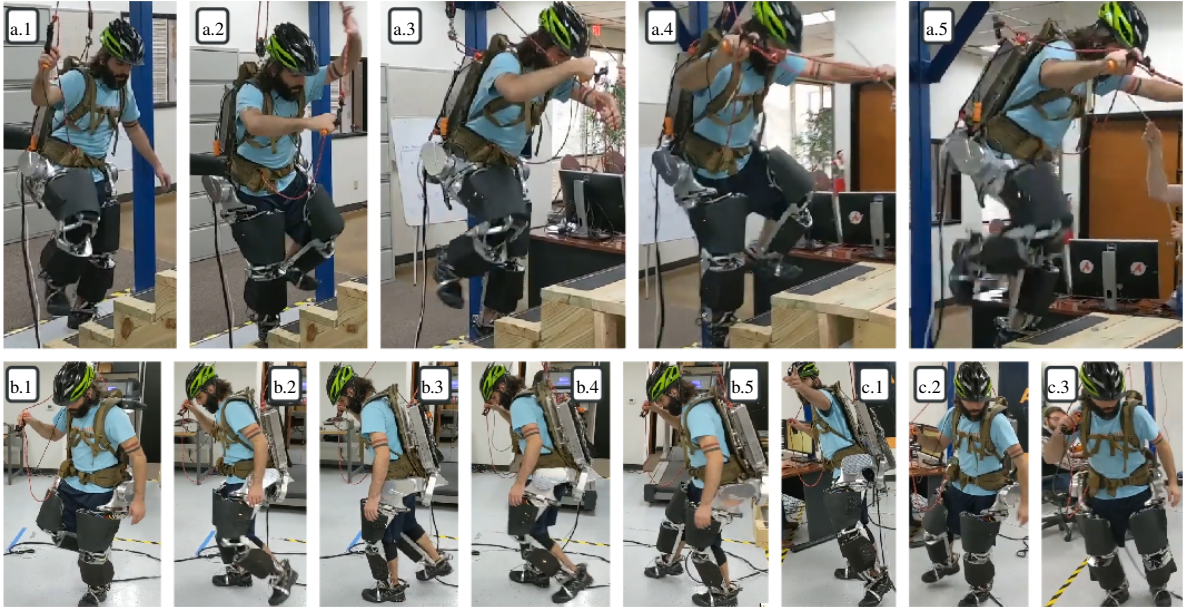


Figure 8. Frames from the demo. Frames a.1-5: climbing stairs with amplification but no added weight. Frames b.1-5: walking around. Frames c.1-3: walking around with amplification and extra weight.

536 Our system is pioneering in that it amplifies human strength at the backpack/hip link of the exoskeleton;
 537 there are no direct performance comparisons for this control feature. Our steady state amplification of human
 538 forces by 300% exceeded the 208% amplification (52% mass reduction) of sagittal hip moment in (Zanotto
 539 et al., 2015), which also used force feedback to amplify human lower-body strength. However, this is not an
 540 exact comparison, as (Zanotto et al., 2015)'s system used a treadmill mounted exoskeleton, had a different
 541 sensing configuration, and has only two degrees of freedom whereas our system has 12. The amplification's
 542 pole frequency (.58 Hz) and amplification magnitude ($\alpha_0 = 3$) at the hip/backpack human–exoskeleton
 543 interface are comparable to our previous results on a 1-DOF human elbow exoskeleton; in the notation
 544 of Appendix A, (He et al., 2019)'s robust controller used $\alpha_0 = 10$, $k_G = 0.1$, $Z_g = 10$, and $P_g = 0.01$,
 545 resulting in an amplification magnitude of 2.995 at 0.58 Hz. However, unlike our controller, (He et al.,
 546 2019) had even greater amplification at lower frequencies: its lowest pole-pair was at 0.146 Hz, and its
 547 steady state amplification rate was 9.91.

548 As shown in Fig. 7's fourth column, the human's effort was reduced to roughly a third of its value in
 549 the third column in the y -torque component. More specifically, the disturbance due to the added weight,
 550 which can be seen by comparing 6.4.3 (with weight) against 6.4.2 (no weight) in terms of y -axis torque, is
 551 attenuated by the amplification factor, resulting in a much smaller disturbance effect when comparing 6.4.4
 552 (attenuated weight) to 6.4.2 (no weight). We must make this comparison despite joint angle differences
 553 on the order of 10 degrees between these tests—a limitation of our operator and operator–exoskeleton
 554 coupling. In 6.4.4, the operator engages in two different squat positions (switching posture at roughly
 555 10 and 20 seconds). The interface forces remain within 10–15 Nm despite these kinematic changes. This
 556 supports the notion that if the operator were able to perfectly reproduce the posture from Exp. 6.4.3 in
 557 6.4.4, the y -axis torque would also be within this range.

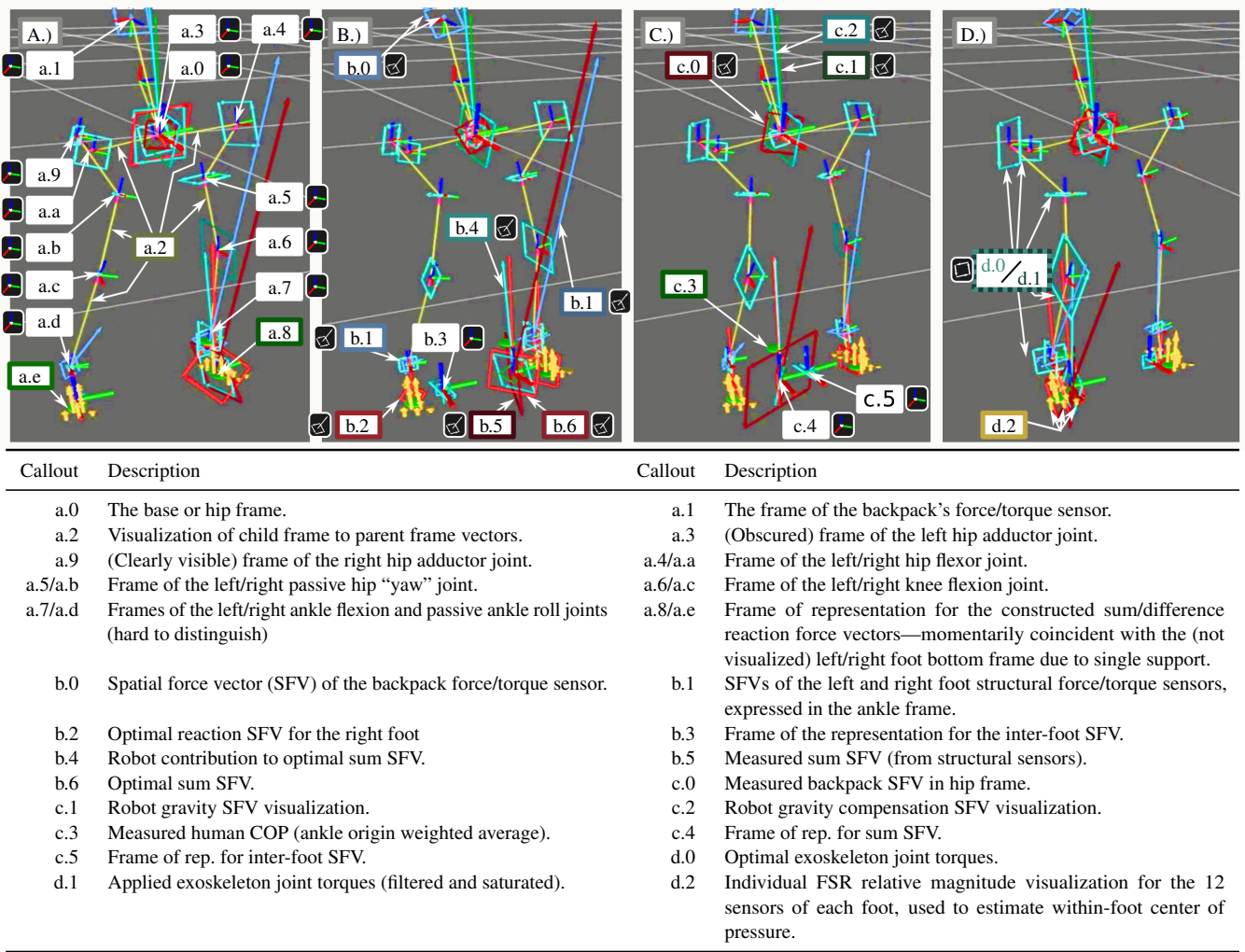


Figure 9. Human weight transfer in 0.2 seconds (subfigures evenly spaced in time) showing the exoskeleton visualization in the rviz program.

558 6.5 Demonstrating Foot Transitions

559 Distributing weight between the two feet using the *inter-foot force task* is a key behavior of the system
 560 and was tested when the operator walked on level ground and stairs. Since the exoskeleton itself was
 561 based on high bandwidth torque-controlled actuation, the operator could easily backdrive it to climb up
 562 stairs or to stand on one foot. While this happened, the exoskeleton continued to compensate for its own
 563 gravitational weight and amplify strength at the hip/backpack sensor.

564 Fig. 8.b and Fig. 9 show the operator shifting weight from one foot to another and lifting up the legs
 565 one at a time. Since the operator decreases the ground reaction force on a foot before lifting it, matching
 566 the measured human ground reaction force distribution between the feet leads the exoskeleton to reduce
 567 its own ground reaction force on that foot in anticipation of the loss of contact. As mentioned in Sec. 4,
 568 the weighting matrices Q_1 and Q_2 in (15) are scheduled according to the exoskeleton's measurement of
 569 the human's weight distribution. When the human shifts weight to one foot, the Q matrix penalty for
 570 reaction forces on the other foot becomes much larger. And since this causes the COP of the exoskeleton to
 571 approximate the COP of the human, this prevents the human from needing to lift a load-bearing exoskeleton
 572 leg. In addition, the penalty limit method allowed the exoskeleton more freedom during dual support but

573 smoothly reduced this freedom when approaching single support, so that by the time it was reached the
574 *inter-foot force task* was essentially the highest priority.

575 This behavior is shown in more detail through the internal exoskeleton visualization of Fig. 9. This Rviz
576 model visualizes many signals of interest, as described in the legend table. All frames are expressed as
577 red (x) green (y) blue (z) line segments meeting at the local origin. Spatial force vectors (comprising a
578 force and a torque) are shown as a ray from the local origin (the force) and a bi-vector—a directed plane
579 comprised of four vectors making a square—to represent the torque. Joint torques are represented as pure
580 bi-vectors. Unlike vector descriptions of torque, the bi-vector visualization has an unambiguous scaling
581 relative to the force visualizations and cannot be confused for them. The four instants pictured in Fig. 9
582 of the contact transition show the apparent center of pressure moving from the left foot to the right foot,
583 and the corresponding shift in all the joint torques and the predicted reaction forces from the shared-body
584 controller. As this is shifting, the reference frame of expression for the sum of reaction forces and the
585 *inter-foot force task*'s difference of reaction forces swap feet. At all times, the reaction force/torque b.6
586 representing the sum is roughly equal to the sum ground reaction force calculated without using the passive
587 joints b.4—which means that the exoskeleton is supporting the vast majority of its weight even during this
588 transition. The backpack force/torque sensor b.0 confirms this, as it is small (and therefore hard to spot)
589 throughout the transition.

7 DISCUSSION

590 Strength amplification control offers us the potential to feel stronger as we manipulate the load through
591 our exoskeleton. This paper deploys a control that has put that vision into practice under laboratory
592 circumstances.

593 7.1 Benefits and Drawbacks

594 This controller has several advantages relative to the state of the art. It respects contact limitations—
595 guaranteeing that the exoskeleton will never force the person to roll their ankles, lift their toes, or slide their
596 feet. It improves human-side admittance relative to the gravity compensation baseline without the anti-
597 stable acceleration feedback of (Kazerooni et al., 2005). It keeps the human in control of the inter-foot force
598 distribution using an elegant linear algebraic decomposition of the contact forces—a more general approach
599 than Ref. (Jacobsen and Olivier, 2014). It allows the operator to move heavy objects without removing the
600 force-feedback path that they would need in order to move the objects carefully—a force-feedback path
601 that is removed by admittance control strategies (Fontana et al., 2014).

602 Of course, the controller has downsides as well. The strategy depends on centralizing the contact between
603 the human and the exoskeleton into a small set of sensors.¹¹ This centralization places a significant burden
604 on the mechanical design and introduces a new failure mode—the “force leak,” where interaction between
605 the exoskeleton and the operator occurs outside the sensors. Additionally, all amplified interaction with
606 the load must go through the exoskeleton structure—another mechanical design challenge. Due to the
607 complexity of the mechanical design problem, the strategy makes it difficult to achieve the ultra-high
608 energy density of successful locomotion augmentation exoskeletons (Kim et al., 2019; Mooney et al., 2014).
609 This is an open problem. Augmentation exoskeletons are already close to the energy-density boundary at
610 which the energy they provide is equal to the energy they cost the user due to their mass. The extra design

¹¹ With one foot on the ground, our exoskeleton measures the human at two places: the hip/backpack attachment and the swing foot attachment.

611 constraints make it harder for amplification exoskeletons to cross this boundary even at slow walking
612 speeds.

613 7.2 Open Problems in the Control Framework

614 The control framework itself also has some open questions. First, we approximated the mechanical
615 impedance of the human and the cuff as being component-wise decoupled between the six degrees of
616 freedom in our *amplification task*. Since an extremely low amplification bandwidth is still stable, and
617 since our tuning process increases bandwidth until instability is discovered, this approximation limits us
618 by introducing conservatism in the final tuning. Because of inter-component human coupling behavior,
619 the tuning process may result in a different answer depending on the order with which the individual task
620 sub-component bandwidths are tuned.

621 Second, the framework was only tested with six *amplification task* sub-components. In theory, it supports
622 arbitrarily many task sub-components. And it is also theoretically possible to join the *inter-foot force*
623 *task* with the *amplification task*—to make the swing foot capable of acting like an amplified manipulator.
624 Elimination of the inter-foot force f_d currently restricts the exoskeleton to applying a pair of ground
625 reaction forces inside a six-dimensional space. The six-dimensional null space that is prohibited includes
626 non-zero internal forces along the axis between the feet and canceling vertical torques perpendicular to
627 the ground—the internal forces of multi-contact (Sentis et al., 2010). If these internal forces were instead
628 amplified, then the exoskeleton could theoretically assist in kicking and manipulation of objects with
629 the feet. We lacked the sensing configuration for such a test: it would require the full 6-DOF interaction
630 force/torque between the human foot and the exoskeleton foot to be measured, rather than just the vertical
631 pressure between them. Thus, to validate the scalability our theory predicts, we would need an exoskeleton
632 with either A) more sensorized human contacts (arms, for example) or B) the elimination of all human–load
633 contact that does not pass through the exoskeleton as an intermediary.

634 Third, the controller tuning process is intended to be robust to all activities the operator performs, but we
635 cannot know all these activities beforehand. A practical extension to this work would be to introduce an
636 always-online learning process to continually adapt the tuning and avoid instability. Previously we have
637 looked at tuning automation using online stiffness estimation (Huang et al., 2020). However, this type of
638 automation could potentially be simpler: if the system starts to vibrate, it could reduce the amplification
639 bandwidth until the vibration subsides. Such a procedure would essentially automate our manual tuning
640 approach.

641 On the other hand, higher performance might be obtained with a more complex strategy: modeling the
642 human and redesigning the controller. Modeling the human online could exploit convex programs that
643 automatically learn bounded-uncertainty models (Thomas and Sentis, 2019). With this more versatile
644 system identification approach, even a human stiffness with ‘off-diagonal’ terms could be learned. With
645 every change to the model of the human stiffness bounds, robust control theory could synthesize a transfer
646 matrix $\mathbf{K}(s)$ that guarantees stability.

647 Relating to the approximate lexicographic optimization using the 1-norm cost, other cost functions
648 could also be considered. In particular, a 2-norm cost approach could smoothly transition through priority
649 inversion events—improving over the hard-switching behavior of the 1-norm cost. Such a cost has been
650 explored in (Campbell, 2018) for this exoskeleton and in (Kim et al., 2020) for biped robots. However,
651 such a cost did not realize a task priority, which hindered efforts to understand the required sacrifices when
652 executing a behavior. Perhaps a generalizing compromise exists in costs that are locally quadratic, but
653 asymptotically linear.

Finally, the approach makes an assumption that a foot is always on the ground—and this precludes interesting applications in free-fall, underwater (with neutral buoyancy), or micro-gravity. In such circumstances, the *amplification task* and *inter-foot force task* structures would need to be combined together and significantly altered. A “virtual single foot contact” would not exist. In its place, the *change in centroidal momentum* (Koolen et al., 2016) would need to become the component of torque-space left intentionally unconstrained by the tasks. The remaining DOFs in torque-space would then be the subject of the new combined amplification task. The assignment of intuitive and easy-to-tune amplification controllers to such a task—which would concern an ever-changing subspace of the end effector contact force space—is an open problem. However, the approach to parameterizing the *internal forces of multi-contact* from (Sentis et al., 2010) would be a reasonable starting point.

7.3 Series Elastic Actuators

Our exoskeleton hardware features series elastic actuators that are force/torque-controlled, and this decision also comes with benefits and drawbacks. To our knowledge, this paper is the first demonstration of Multi-DOF amplification control based on human interface force sensors and actuator force sensors (i.e. the series elastic elements). While such actuators are commonly used in wearable robots, they are a key part of our strategy, because with them we can avoid sensorizing the external force interface. This is a major advantage compared to systems designed to follow the extender concept (Kazerooni and Guo, 1993). The lack of load sensors gives us the freedom to properly handle amplification for load contract forces at any contact point along the structure of the exoskeleton.

As for series compliance itself, however, control performance would be *better* with nearly-rigid springs. In our experiment, the primary bandwidth-limiting factor that $\eta(s)$ must describe is the 10 Hz bandwidth of the exoskeleton’s actuators. And this bandwidth is limited by the mechanical stiffness of the series spring, the noise level in the motor position and spring deflection sensors, and the bandwidth of the low-level electrical current controller. The time-delay of approximately 1 ms was non-limiting (due to the 10 Hz actuator bandwidth), so to improve the overall performance of the exoskeleton, the most efficient strategy would be to increase the spring stiffness and spring deflection sensor resolution. The series elastic actuators are simply torque sources to us, and direct drive motors offer higher bandwidth as torque sources. Removing the springs could also save weight. But series elasticity has some practical advantages: the force sensing is cheap and high quality, the exoskeleton’s motors are protected from impacts, and both the transmission’s friction and the rotor’s reflected inertia are well hidden from the user.

7.4 Potential Applications

We have demonstrated the control framework on the Apptronik Sagittarius exoskeleton, which is designed to lift heavy payloads as the user moves quickly. In this use case, the benefit of amplification control—relative to gravity compensation of the payload—is the potential reduction of inertial forces the user needs to compensate (without resorting to acceleration feedback) and the forces due to modeling error in the compensation. Future controllers for this application might investigate further enhancements to the operator’s quality of life, such as posture or safety support that guides the user.

However, amplification is also of great interest in load manipulation and heavy-duty tool use. We imagine some industrial amplification exoskeletons might be for slowly manipulating very large loads under direct human control. If they were to move fast, they would require significantly more impressive power density than we typically see today. Such an exoskeleton, worn by a skilled operator, might be fielded in difficult terrain as an alternative to tracked construction vehicles, perhaps with specialized tools for manipulating

696 the environment. Given the strength of the system, these tools might not be constrained by weight relative
697 to other tools for such difficult environments. The exoskeleton could act as an adjustable bracing system
698 that allows the operator to maneuver them into position in a controlled way. For example, a construction
699 worker could use an exoskeleton to maneuver an oversize pneumatic drill to carve a staircase on un-finished
700 mountain terrain. Exoskeletons as platforms offer new possibilities for industrial tools and potential job
701 sites by combining the flexibility of people with the strength of machines.

702 While our exoskeleton is designed to mimic the kinematics of the person wearing it, this is not the only
703 way to approach the design. The control framework also has the potential to allow non-anthropomorphic
704 exoskeletons to amplify human interaction. For example, consider a robot connected to an operator's feet
705 with long spindly legs that join together at a robot 'hip'. Where this hip also features an enormous power
706 tool that requires the user to manipulate it with both hands. Such an architecture would require the same
707 control system features as our anthropomorphic exoskeleton structure: strength amplification in the frame
708 of the robot's hip, awareness of contact inequalities, and human-led footstep transitions.

ACKNOWLEDGMENT

709 For this research in human strength amplification, Apptronik Systems Inc. provided, at no cost, access to
710 their exoskeleton hardware called Sagit-P5. They also provided mechanical maintenance and improvements
711 to the low level interfaces to facilitate the testing. The authors would like to thank Donghyun Kim for
712 providing insights on contact transitions. This system was designed and built by a team including Jonas
713 Fox, Brad Resh, Uday Savaria, Ryan Harkins, Ryan MacWilliams, Joel Cox, and Paul Fleury. The authors
714 would also like to acknowledge Bill Helmsing and Jeff Cardenas for allocating time for our research on the
715 Sagit-P5 exoskeleton.

716 This work was supported in part by NASA grant NNX15AQ33H "Controlling Robots with a Spring in
717 Their Step," for which Gray Thomas is the fellow and Luis Sentis is the advisor and by two STTR grants
718 from the US Department of Defense.

REFERENCES

- 719 Adams, R. J. and Hannaford, B. (1999). Stable haptic interaction with virtual environments. *IEEE*
720 *Transactions on Robotics and Automation* 15, 465–474
- 721 Agrawal, A., Harib, O., Hereid, A., Finet, S., Masselin, M., Praly, L., et al. (2017). First steps towards
722 translating hzd control of bipedal robots to decentralized control of exoskeletons. *IEEE Access* 5,
723 9919–9934
- 724 Bouyarmane, K. and Kheddar, A. (2017). On weight-prioritized multitask control of humanoid robots.
725 *IEEE Transactions on Automatic Control* 63, 1632–1647
- 726 Bretl, T. and Lall, S. (2008). Testing static equilibrium for legged robots. *IEEE Transactions on Robotics*
727 24, 794–807
- 728 Brissonneau, N., He, B., Thomas, G. C., and Sentis, L. (2021). Biologically-inspired impedance control
729 with hysteretic damping. *IEEE Control Systems Letters* 5, 1717–1722. doi:10.1109/LCSYS.2020.
730 3044101
- 731 Buerger, S. P. and Hogan, N. (2006). Relaxing passivity for human-robot interaction. In *Intelligent Robots*
732 and *Systems (IROS), 2006 IEEE/RSJ International Conference on* (IEEE), 4570–4575
- 733 Buerger, S. P. and Hogan, N. (2007). Complementary stability and loop shaping for improved human–robot
734 interaction. *IEEE Transactions on Robotics* 23, 232–244. doi:10.1109/TRO.2007.892229

- 735 Campbell, O. H., IV (2018). *Framework for Full Body Augmentative Exoskeleton Control*. Master's thesis,
736 The University of Texas at Austin
- 737 Candes, E. J., Wakin, M. B., and Boyd, S. P. (2008). Enhancing sparsity by reweighted ℓ_1 minimization.
738 *Journal of Fourier analysis and applications* 14, 877–905
- 739 Colgate, J. E. and Brown, J. M. (1994). Factors affecting the z-width of a haptic display. In *Robotics and*
740 *Automation, 1994. Proceedings., 1994 IEEE International Conference on* (IEEE), 3205–3210
- 741 Colgate, J. E. and Hogan, N. (1988). Robust control of dynamically interacting systems. *International*
742 *Journal of Control* 48, 65–88
- 743 Featherstone, R. (2014). *Rigid body dynamics algorithms* (Springer)
- 744 Fontana, M., Vertechy, R., Marcheschi, S., Salsedo, F., and Bergamasco, M. (2014). The body extender:
745 A full-body exoskeleton for the transport and handling of heavy loads. *IEEE Robotics & Automation*
746 *Magazine* 21, 34–44
- 747 Gonzalez, D. J. and Asada, H. H. (2019). Hybrid open-loop closed-loop control of coupled human–robot
748 balance during assisted stance transition with extra robotic legs. *IEEE Robotics and Automation Letters*
749 4, 1676–1683
- 750 He, B., Huang, H., Thomas, G. C., and Sentis, L. (2019). Complex stiffness model of physical human-robot
751 interaction: Implications for control of performance augmentation exoskeletons. In *2019 IEEE/RSJ*
752 *International Conference on Intelligent Robots and Systems (IROS)* (IEEE), 6748–6755
- 753 He, B., Huang, H., Thomas, G. C., and Sentis, L. (2020). A complex stiffness human impedance model with
754 customizable exoskeleton control. *IEEE Transactions on Neural Systems and Rehabilitation Engineering*
755 28, 2468–2477
- 756 He, B., Thomas, G. C., Paine, N., and Sentis, L. (2019). Modeling and loop shaping of single-joint
757 amplification exoskeleton with contact sensing and series elastic actuation. In *2019 Annual American*
758 *Control Conference (ACC)*. AACC (IEEE), 4580–4587
- 759 Hogan, N. (1984). Adaptive control of mechanical impedance by coactivation of antagonist muscles. *IEEE*
760 *Transactions on Automatic Control* 29, 681–690
- 761 Hogan, N. (1989). Controlling impedance at the man/machine interface. In *Robotics and Automation*
762 *(ICRA), 1989 IEEE International Conference on* (IEEE), 1626–1631
- 763 Huang, H., Cappel, H., Thomas, G. C., He, B., and Sentis, L. (2020). In *2020 Annual American Control*
764 *Conference (ACC)*. AACC (IEEE), 5131–5138
- 765 Jacobsen, S. C. and Olivier, M. X. (2014). *Contact displacement actuator system*. US Patent 8,849,457
- 766 Kawamoto, H. and Sankai, Y. (2005). Power assist method based on phase sequence and muscle force
767 condition for hal. *Advanced Robotics* 19, 717–734
- 768 Kazerooni, H. (1990). Human-robot interaction via the transfer of power and information signals. *IEEE*
769 *Transactions on Systems, Man, and Cybernetics* 20, 450–463
- 770 Kazerooni, H. (2005). Exoskeletons for human power augmentation. In *Intelligent Robots and Systems*
771 *(IROS), 2005 IEEE/RSJ International Conference on* (IEEE), 3459–3464
- 772 Kazerooni, H. and Guo, J. (1993). Human extenders. *Journal of Dynamic Systems, Measurement, and*
773 *Control* 115, 281–290
- 774 Kazerooni, H. and Mahoney, S. (1991a). Dynamics and control of robotic systems worn by humans. In
775 *Proceedings. 1991 IEEE International Conference on Robotics and Automation* (IEEE), 2399–2405
- 776 Kazerooni, H. and Mahoney, S. L. (1991b). Dynamics and control of robotic systems worn by humans.
777 *Journal of Dynamic Systems, Measurement, and Control* 113, 379–387. doi:10.1115/1.2896421

- 778 Kazerouni, H., Racine, J.-L., Huang, L., and Steger, R. (2005). On the control of the berkeley lower
779 extremity exoskeleton (BLEEX). In *Robotics and Automation (ICRA), 2005 IEEE International
780 Conference on* (IEEE), 4353–4360
- 781 Kim, B. and Deshpande, A. D. (2017). An upper-body rehabilitation exoskeleton harmony with
782 an anatomical shoulder mechanism: Design, modeling, control, and performance evaluation. *The
783 International Journal of Robotics Research* 36, 414–435
- 784 Kim, D., Jorgensen, S. J., Hwang, H., and Sentis, L. (2018). Control scheme and uncertainty considerations
785 for dynamic balancing of passive-ankled bipeds and full humanoids. In *2018 IEEE-RAS 18th
786 International Conference on Humanoid Robots (Humanoids)* (IEEE), 1–9
- 787 Kim, D., Jorgensen, S. J., Lee, J., Ahn, J., Luo, J., and Sentis, L. (2020). Dynamic locomotion for
788 passive-ankle biped robots and humanoids using whole-body locomotion control. *The International
789 Journal of Robotics Research* 39, 936–956
- 790 Kim, D., Zhao, Y., Thomas, G. C., Fernandez, B. R., and Sentis, L. (2016). Stabilizing series-elastic
791 point-foot bipeds using whole-body operational space control. *IEEE Transactions on Robotics* 32,
792 1362–1379
- 793 Kim, J., Lee, G., Heimgartner, R., Arumukhom Revi, D., Karavas, N., Nathanson, D., et al. (2019).
794 Reducing the metabolic rate of walking and running with a versatile, portable exosuit. *Science* 365,
795 668–672. doi:10.1126/science.aav7536
- 796 Kong, K., Moon, H., Jeon, D., and Tomizuka, M. (2010). Control of an exoskeleton for realization of
797 aquatic therapy effects. *IEEE/ASME Transactions on Mechatronics* 15, 191–200
- 798 Kong, K. and Tomizuka, M. (2009). Control of exoskeletons inspired by fictitious gain in human model.
799 *IEEE/ASME Transactions on Mechatronics* 14, 689–698
- 800 Koolen, T., Bertrand, S., Thomas, G. C., De Boer, T., Wu, T., Smith, J., et al. (2016). Design of a
801 momentum-based control framework and application to the humanoid robot Atlas. *International Journal
802 of Humanoid Robotics* 13, 1650007
- 803 Kwa, H. K., Noorden, J. H., Missel, M., Craig, T., Pratt, J. E., and Neuhaus, P. D. (2009). Development of
804 the IHMC mobility assist exoskeleton. In *Robotics and Automation (ICRA), 2009 IEEE International
805 Conference on* (IEEE), 2556–2562
- 806 Lecours, A., St-Onge, B. M., and Gosselin, C. (2012). Variable admittance control of a four-degree-
807 of-freedom intelligent assist device. In *Robotics and Automation (ICRA), 2012 IEEE International
808 Conference on* (IEEE), 3903–3908
- 809 Lin, J., Lv, G., and Gregg, R. D. (2019). Contact-invariant total energy shaping control for powered
810 exoskeletons. In *2019 American Control Conference (ACC)* (AACC), 664–670
- 811 Lougee-Heimer, R. (2003). The common optimization interface for operations research: Promoting
812 open-source software in the operations research community. *IBM Journal of Research and Development*
813 47, 57–66
- 814 Lv, G., Zhu, H., and Gregg, R. D. (2018). On the design and control of highly backdrivable lower-limb
815 exoskeletons: A discussion of past and ongoing work. *IEEE Control Systems Magazine* 38, 88–113
- 816 Makinson, J. B., Bodine, D. P., and Fick, B. R. (1969). *Machine augmentation of human strength and
817 endurance Hardiman I prototype project*. Tech. rep., Specialty Materials Handling Products Operation,
818 General Electric Company
- 819 Mooney, L. M., Rouse, E. J., and Herr, H. M. (2014). Autonomous exoskeleton reduces metabolic cost of
820 human walking during load carriage. *Journal of neuroengineering and rehabilitation* 11, 80
- 821 Mungai, M. E. and Grizzle, J. (2020). Feedback control design for robust comfortable sit-to-stand motions
822 of 3d lower-limb exoskeletons. *IEEE Access*

- 823 Paine, N., Mehling, J. S., Holley, J., Radford, N. A., Johnson, G., Fok, C.-L., et al. (2015). Actuator control
824 for the NASA-JSC Valkyrie humanoid robot: A decoupled dynamics approach for torque control of
825 series elastic robots. *Journal of Field Robotics* 32, 378–396
- 826 Paine, N., Oh, S., and Sentis, L. (2014). Design and control considerations for high-performance series
827 elastic actuators. *IEEE/ASME Transactions on Mechatronics* 19, 1080–1091
- 828 Paine, N. A. (2014). *High-performance series elastic actuation*. Ph.D. thesis, The University of Texas at
829 Austin
- 830 Radford, N. A., Strawser, P., Hambuchen, K., Mehling, J. S., Verdeyen, W. K., Donnan, A. S., et al. (2015).
831 Valkyrie: NASA's first bipedal humanoid robot. *Journal of Field Robotics* 32, 397–419
- 832 Sawicki, G. S., Beck, O. N., Kang, I., and Young, A. J. (2020). The exoskeleton expansion: improving
833 walking and running economy. *Journal of neuroengineering and rehabilitation* 17, 1–9
- 834 Sentis, L., Park, J., and Khatib, O. (2010). Compliant control of multicontact and center-of-mass behaviors
835 in humanoid robots. *Robotics, IEEE Transactions on* 26, 483–501
- 836 Stephens, B. J. and Atkeson, C. G. (2010). Dynamic balance force control for compliant humanoid
837 robots. In *2010 IEEE/RSJ International Conference on Intelligent Robots and Systems*. 1248–1255.
838 doi:10.1109/IROS.2010.5648837
- 839 Sugar, T. G., He, J., Koeneman, E. J., Koeneman, J. B., Herman, R., Huang, H., et al. (2007). Design
840 and control of RUPERT: a device for robotic upper extremity repetitive therapy. *IEEE transactions on*
841 *neural systems and rehabilitation engineering* 15, 336–346
- 842 Thomas, G. C. (2019). *LP Exo: A free implementation of a 1-Norm Prioritized Whole Body Controller*.
843 GitHub, https://bitbucket.org/gray_thomas/exo_lp.git
- 844 Thomas, G. C. (2020). *Implementation of "An Amplification Shaping Framework for Exoskeletal Human*
845 *Strength Augmentation"*. Youtube. https://youtu.be/rcDMHYgGV_4
- 846 Thomas, G. C., Coholich, J. M., and Sentis, L. (2019). Compliance shaping for control of strength
847 amplification exoskeletons with elastic cuffs. In *Proceedings of the 2019 IEEE/ASME International*
848 *Conference on Advanced Intelligent Mechatronics* (IEEE and ASME), 1199–1206
- 849 Thomas, G. C. and Sentis, L. (2019). Quadric inclusion programs: an lmi approach to \mathcal{H}_∞ -model
850 identification. *IEEE Transactions on Automatic Control* 64, 4229–4236. doi:10.1109/TAC.2019.2897886
- 851 Young, A. J. and Ferris, D. P. (2016). State of the art and future directions for lower limb robotic
852 exoskeletons. *IEEE Transactions on Neural Systems and Rehabilitation Engineering* 25, 171–182
- 853 Yu, W. and Rosen, J. (2013). Neural PID control of robot manipulators with application to an upper limb
854 exoskeleton. *IEEE Transactions on Cybernetics* 43, 673–684
- 855 Zanotto, D., Akiyama, Y., Stegall, P., and Agrawal, S. K. (2015). Knee joint misalignment in exoskeletons
856 for the lower extremities: Effects on user's gait. *IEEE Transactions on Robotics* 31, 978–987
- 857 Zhang, J., Fiers, P., Witte, K. A., Jackson, R. W., Poggensee, K. L., Atkeson, C. G., et al. (2017).
858 Human-in-the-loop optimization of exoskeleton assistance during walking. *Science* 356, 1280–1284